nature biomedical engineering

SUPPLEMENTARY INFORMATION

https://doi.org/10.1038/s41551-020-0584-z

In the format provided by the authors and unedited.

Gold/alpha-lactalbumin nanoprobes for the imaging and treatment of breast cancer

Jiang Yang[1,2,3], Tai Wang[4], Lina Zhao[5], Vinagolu K. Rajasekhar[6], Suhasini Joshi[4], Chrysafis Andreou[1,2], Suchetan Pal[1,2], Hsiao-ting Hsu[1,2], Hanwen Zhang[1,2], Ivan J. Cohen[1,7], Ruimin Huang[1,2], Ronald C. Hendrickson[8], Matthew M. Miele[8], Wenbo Pei[4], Matthew B. Brendel[9], John H. Healey[6], Gabriela Chiosis[4,10] and Moritz F. Kircher[1,2,11,12,13,14] ✉

[1]Center for Molecular Imaging and Nanotechnology (CMINT), Memorial Sloan Kettering Cancer Center, New York, NY, USA. [2]Department of Radiology, Memorial Sloan Kettering Cancer Center, New York, NY, USA. [3]State Key Laboratory of Oncology in South China, Collaborative Innovation Center for Cancer Medicine, Sun Yat-sen University Cancer Center, Guangzhou, China. [4]Chemical Biology Program, Sloan Kettering Institute, New York, NY, USA. [5]CAS Key Laboratory for Biomedical Effects of Nanomaterials and Nanosafety, Institute of High Energy Physics, Chinese Academy of Sciences, Beijing, China. [6]Department of Surgery, Memorial Sloan Kettering Cancer Center, New York, NY, USA. [7]Louis V. Gerstner Jr Graduate School of Biomedical Sciences, Memorial Sloan Kettering Cancer Center, New York, NY, USA. [8]Proteomics and Microchemistry Core Laboratory, Memorial Sloan Kettering Cancer Center, New York, NY, USA. [9]Molecular Cytology Core Laboratory, Memorial Sloan Kettering Cancer Center, New York, NY, USA. [10]Breast Cancer Service, Department of Medicine, Memorial Sloan Kettering Cancer Center, New York, NY, USA. [11]Molecular Pharmacology Program, Sloan Kettering Institute, New York, NY, USA. [12]Department of Radiology, Weill Cornell Medical College, New York, NY, USA. [13]Department of Imaging, Dana-Farber Cancer Institute and Harvard Medical School, Boston, MA, USA. [14]Department of Radiology, Brigham & Women's Hospital and Harvard Medical School, Boston, MA, USA. ✉e-mail: moritz_kircher@dfci.harvard.edu

Table of Contents

Supplementary Video 1 caption:
Time-lapse differential interference contrast (DIC) microscopic imaging of MDA-MB-231 cancer cells treated with $AuQC_{705}$-BAMLET

Supplementary Video 2 caption:
Time-lapse DIC imaging of MDA-MB-231 cancer cells treated with PBS

Supplementary Video 3 caption:
Time-lapse DIC imaging of MDA-MB-231 cancer cells treated with α-LA

Supplementary Video 4 caption:
Time-lapse DIC imaging of MDA-MB-231 cancer cells treated with $AuQC_{705}$

Supplementary Figures

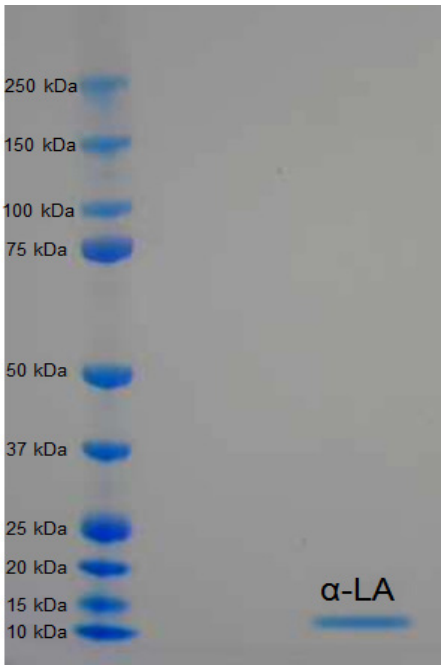

Supplementary Fig. 1 | Sodium dodecyl sulfate-polyacrylamide gel electrophoresis (SDS-PAGE) of the source alpha-lactalbumin (α-LA). Coomassie Brilliant Blue staining with molecular-weight protein ladders showed a single protein band of bovine α-LA around 14 kDa.

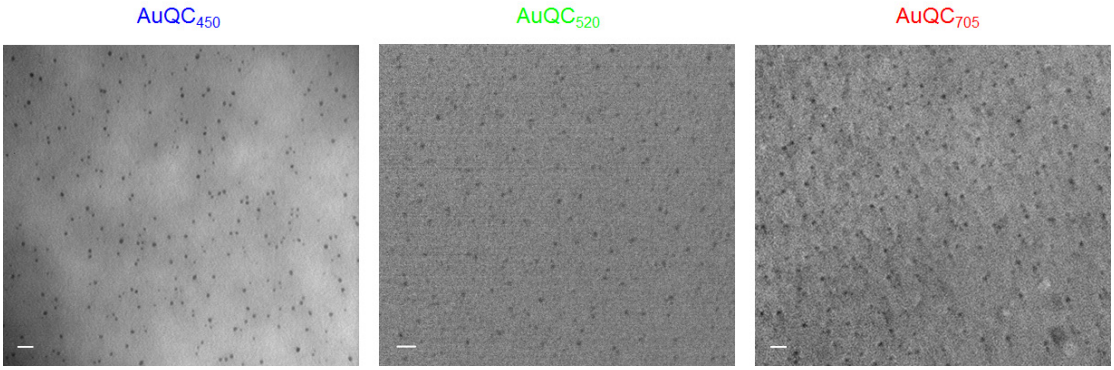

Supplementary Fig. 2 | Transmission electron microscopic (TEM) images of gold quantum clusters (AuQCs). All AuQCs showed monodispersed ultrasmall sizes. Scale bars: 10 nm.

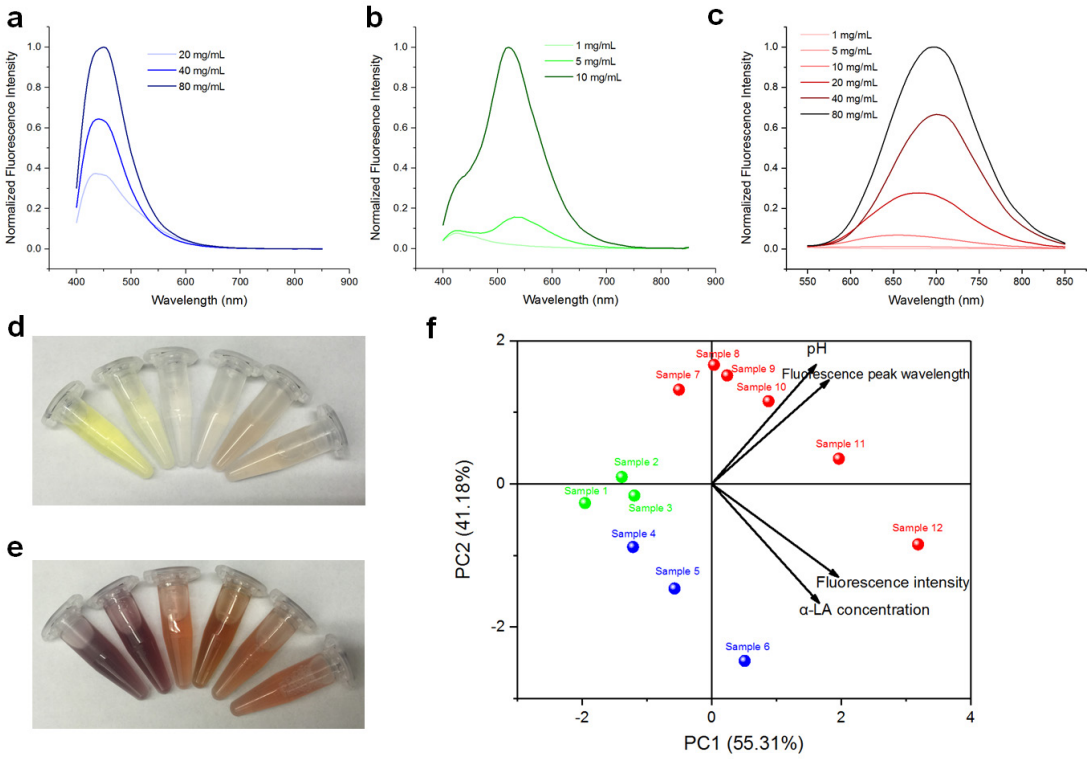

Supplementary Fig. 3 | Fluorescence of AuQCs synthesized under different conditions. Synthesis was conducted with α-LA concentrations of **(a)** 20-80 mg/mL (sample 4-6) and **(b)** 1-10 mg/mL (sample 1-3) under acidic conditions, **(c)** 1-80 mg/mL (sample 7-12) under alkaline conditions. Excitation wavelength: 360 nm. Photographs of AuQCs synthesized with α-LA concentrations of 1-80 mg/mL (left to right) under **(d)** acidic and **(e)** alkaline conditions. High α-LA concentrations at alkaline pH were observed to bathochromically shift fluorescence emission to the near-infrared (NIR) region with increased intensity. Reactions in all conditions progressed at 40°C for identical 20 h under vigorous mixing. **(f)** Principal component analysis (PCA) plot of AuQCs synthesized under different conditions. 96.5% cumulative variances were explained by the first two components. PCA loadings revealed that fluorescence emission wavelength is strongly correlated with pH (R=0.896) while the intensity is mainly decided by α-LA concentrations (R=0.937).

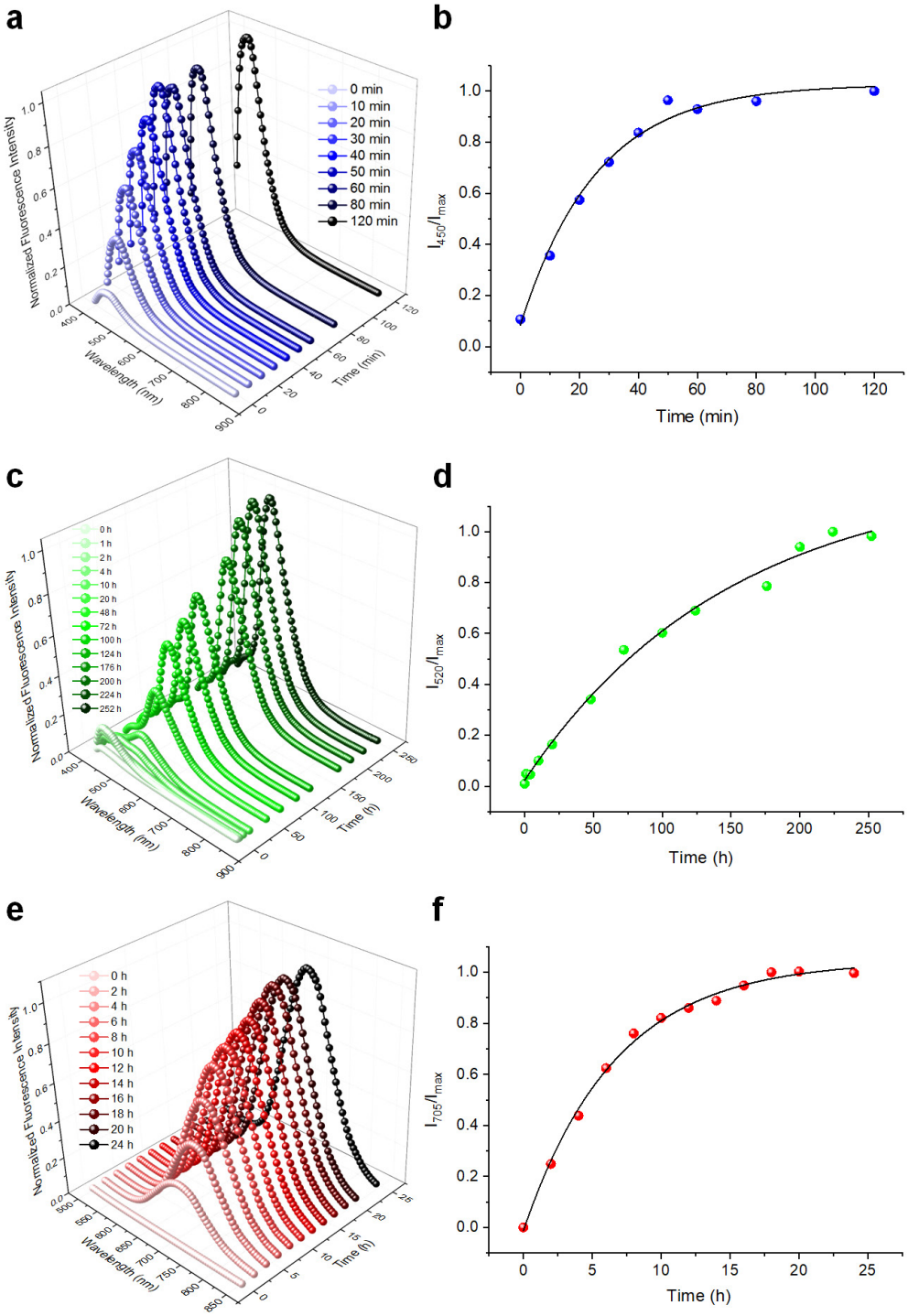

Supplementary Fig. 4 | Time evolution profiles of fluorescence emissions for AuQCs. **(a)** $AuQC_{450}$, **(c)** $AuQC_{520}$ and **(e)** $AuQC_{705}$ were synthesized at 40°C with fluorescence monitored periodically. Corresponding peak intensity-time correlations were shown in **b, d** and **f**, respectively.

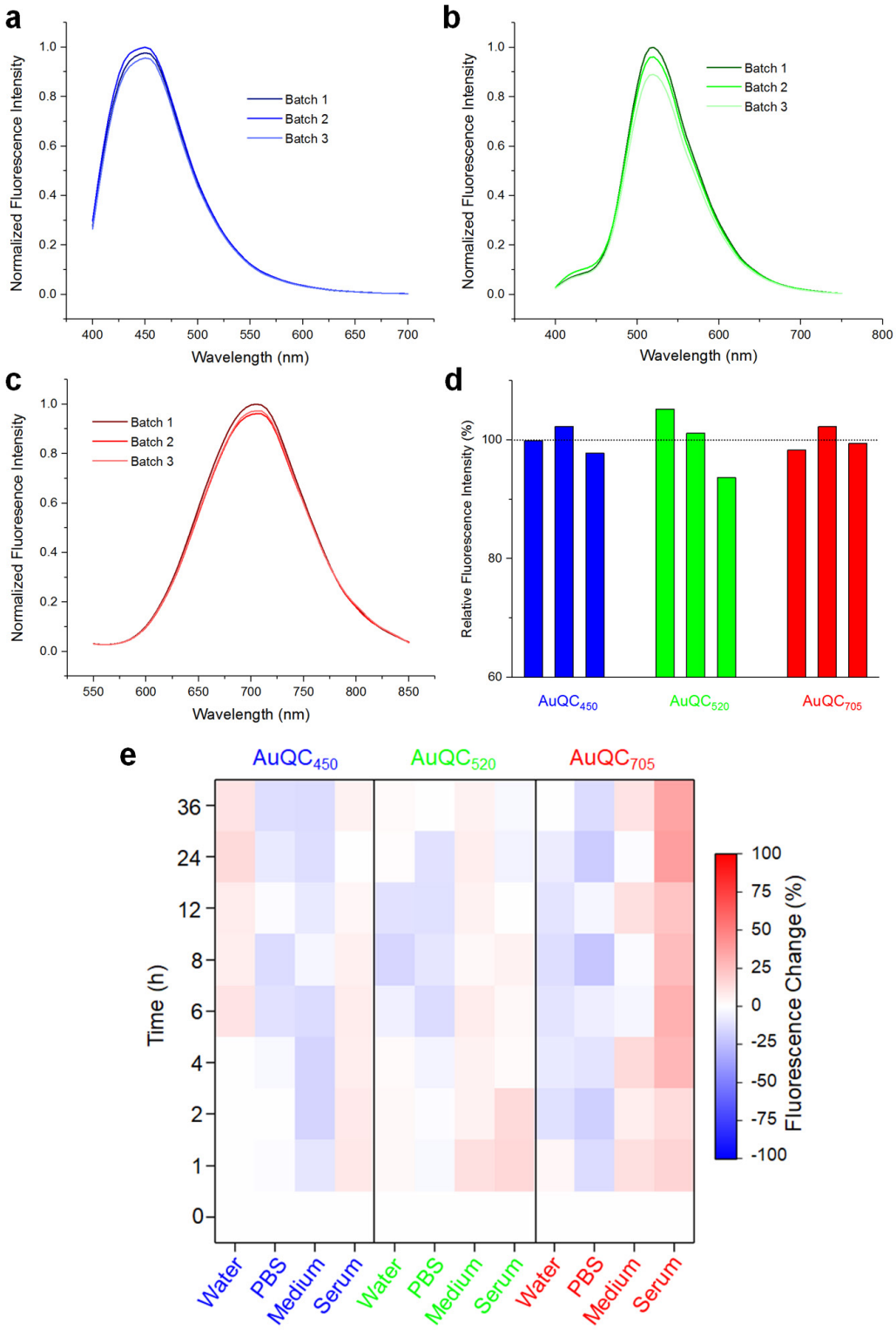

Supplementary Fig. 5 | Reproducibility and stability of AuQCs. **(a-c)** Fluorescence spectra of 3 individually synthesized batches of $AuQC_{450}$, $AuQC_{520}$ and $AuQC_{705}$. **(d)** Deviations from the mean. **(e)** Fluorescence stabilities of AuQCs in DI water, PBS, 50% RPMI medium and 50% mouse serum at 37°C. The variability is <±35% under all conditions.

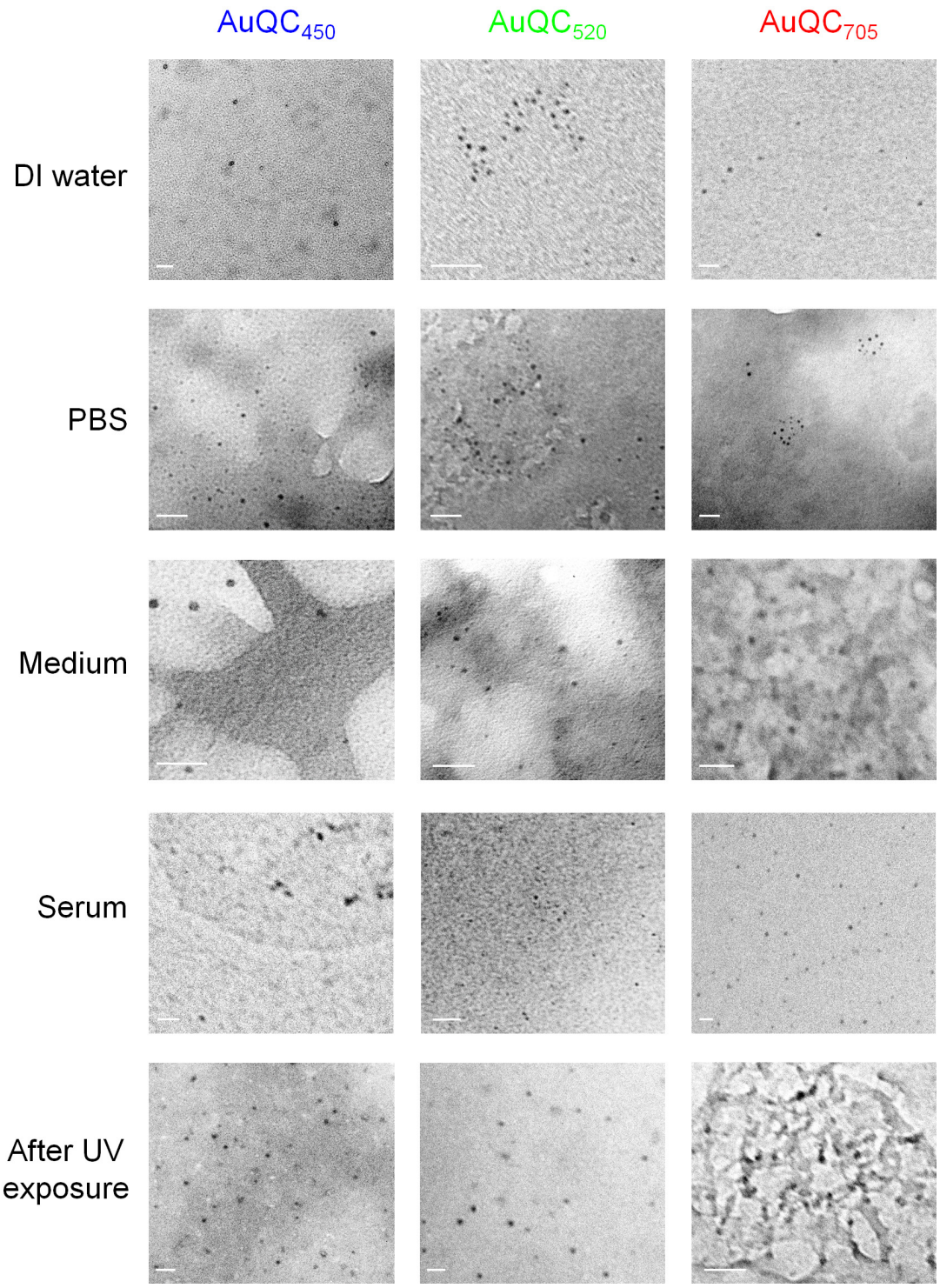

Supplementary Fig. 6 | TEM images of AuQCs after incubation at various conditions. AuQCs were incubated in DI water, PBS, 50% RPMI medium, 50% mouse serum at 37°C for 36 h or after 1 h continuous exposure to UV irradiation. AuQCs showed sufficient stability and maintained their ultrasmall size. Scale bars: 20 nm.

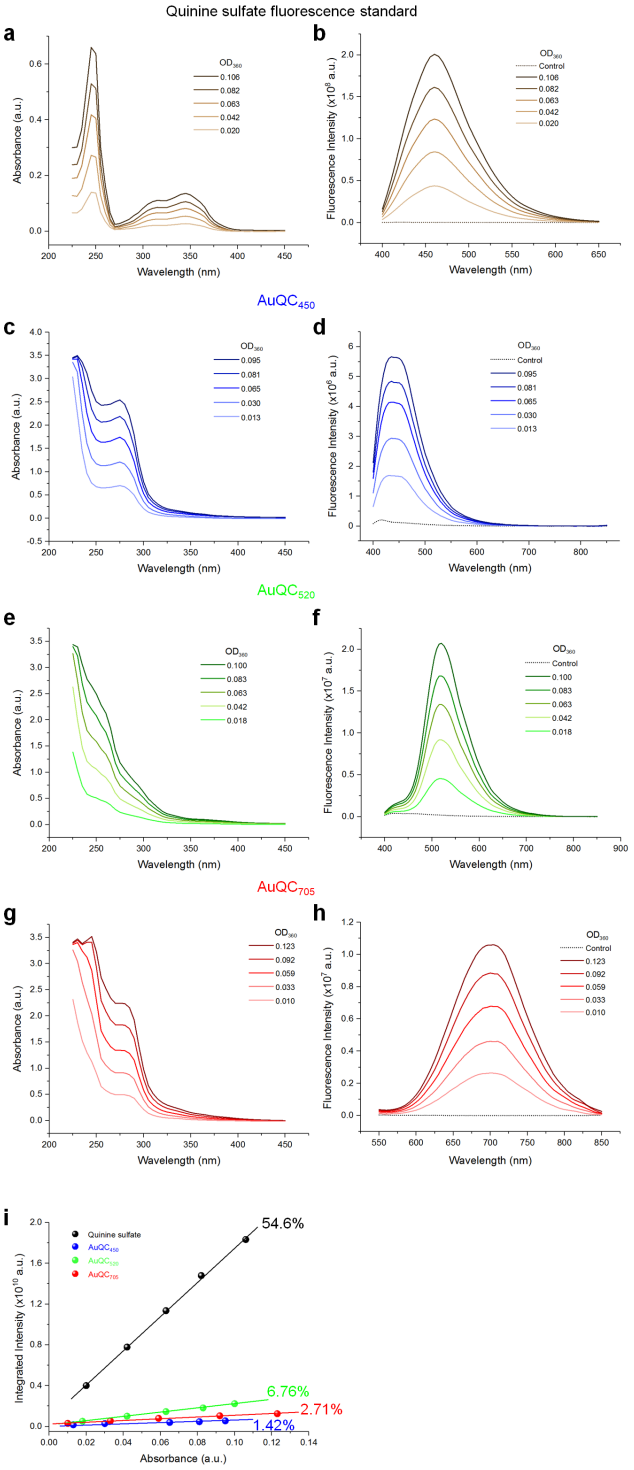

Supplementary Fig. 7 | Quantum yields (QYs) of AuQCs. Absorbance and fluorescence, respectively, of **(a-b)** quinine sulfate, **(c-d)** $AuQC_{450}$, **(e-f)** $AuQC_{520}$, and **(g-h)** $AuQC_{705}$. The optical density (OD) in each spectrum corresponds to the absorbance at 360 nm. **(i)** Plot of integrated fluorescence intensities and absorbance for quinine sulfate and AuQCs for QY calculations derived from slopes of linear fits.

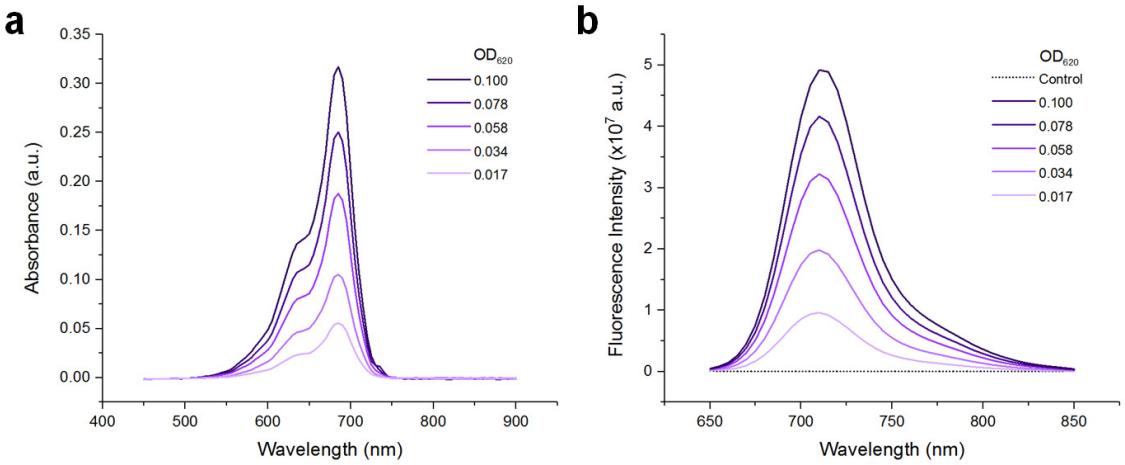

Supplementary Fig. 8 | Quantum yield of $AuQC_{705}$ with reference to Cy5.5-*N*-hydroxysuccinimide (NHS). (a) Absorbance and **(b)** fluorescence spectra of Cy5.5-NHS ester as the fluorescence reference standard. This non-sulfonated dye has an emission wavelength comparable to $AuQC_{705}$ in the NIR region and a QY of 20% in dimethyl sulfoxide (DMSO). The relative QY of $AuQC_{705}$ was measured to be 4.70%.

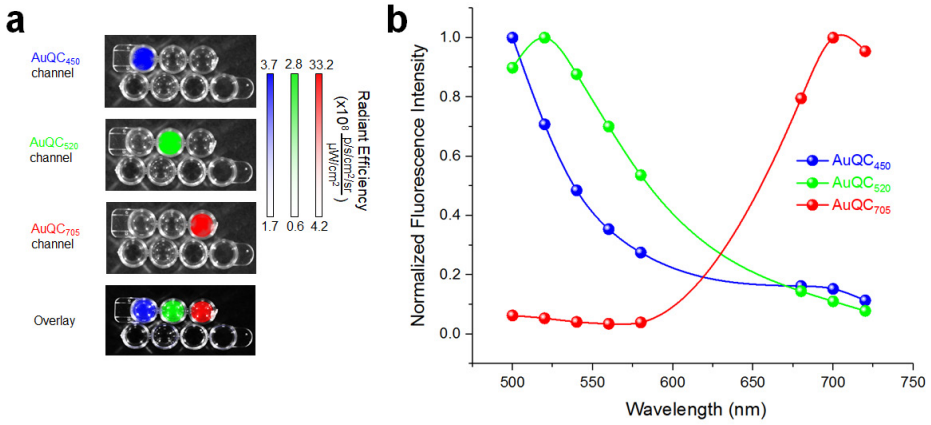

Supplementary Fig. 9 | Fluorescence phantom images of AuQCs. (a) Fluorescence of $AuQC_{450}$, $AuQC_{520}$ and $AuQC_{705}$ excited by the same excitation was coded as blue, green and red respectively. Phantom layout (left to right): $AuQC_{450}$, $AuQC_{520}$ and $AuQC_{705}$ (top); DI water, α-LA, $HAuCl_4$ precursor and blank (bottom). **(b)** Corresponding in vitro multispectral fluorescence spectra of AuQCs.

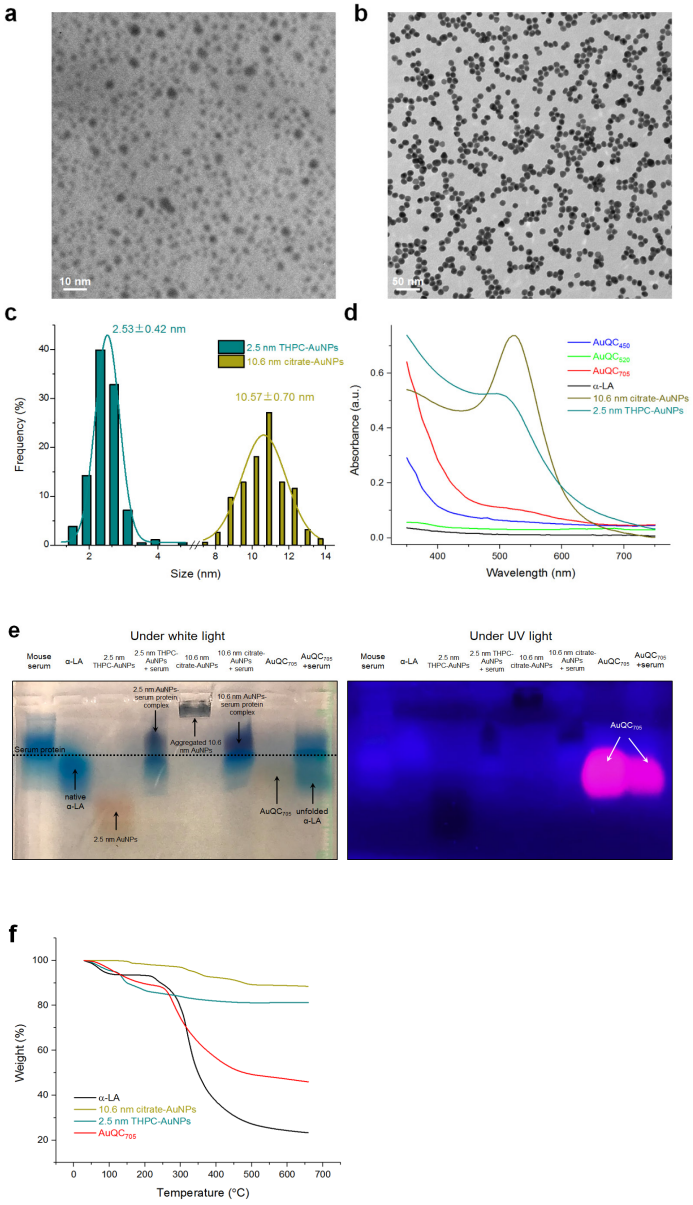

Supplementary Fig. 10 | Comparison of AuQCs to gold nanoparticles (AuNPs). TEM images of **(a)** 2.5 nm ultrasmall tetrakis(hydroxymethyl) phosphonium chloride (THPC)-capped and **(b)** 10.6 nm citrate-capped AuNPs. **(c)** Corresponding size distribution histograms. **(d)** UV-vis absorption spectra of AuQCs, native α-LA, 10.6 nm citrate-capped and 2.5 nm THPC-capped AuNPs. **(e)** Agarose gel electrophoresis of 2.5 nm THPC-AuNPs, 10.6 nm citrate-AuNPs and $AuQC_{705}$ after 1 h incubation with 10% mouse serum at 37°C. Coomassie Brilliant Blue G-250 was used to visualize proteins. $AuQC_{705}$ control without serum incubation was loaded at a 2-fold concentration (1.5 mg/mL) to show better band contrast under white light. 10.6 nm citrate-AuNPs are unstable with strong aggregations at the loading well. Both 2.5 nm and 10.6 nm conventional AuNPs show strong binding to serum proteins and form protein corona complexes, but $AuQC_{705}$ has minimal serum binding with the fluorescence band almost at the same position after incubation in serum. The position of the electrophoretic protein band of α-LA from $AuQC_{705}$ suggested its partially unfolded state as compared to native α-LA. **(f)** Thermogravimetric analysis (TGA) curves of 2.5 nm ultrasmall THPC-capped,10.6 nm citrate-capped AuNPs and $AuQC_{705}$. Due to the involvement of α-LA during synthesis, $AuQC_{705}$ shows a much larger thermally degradable organic content compared to conventional AuNPs.

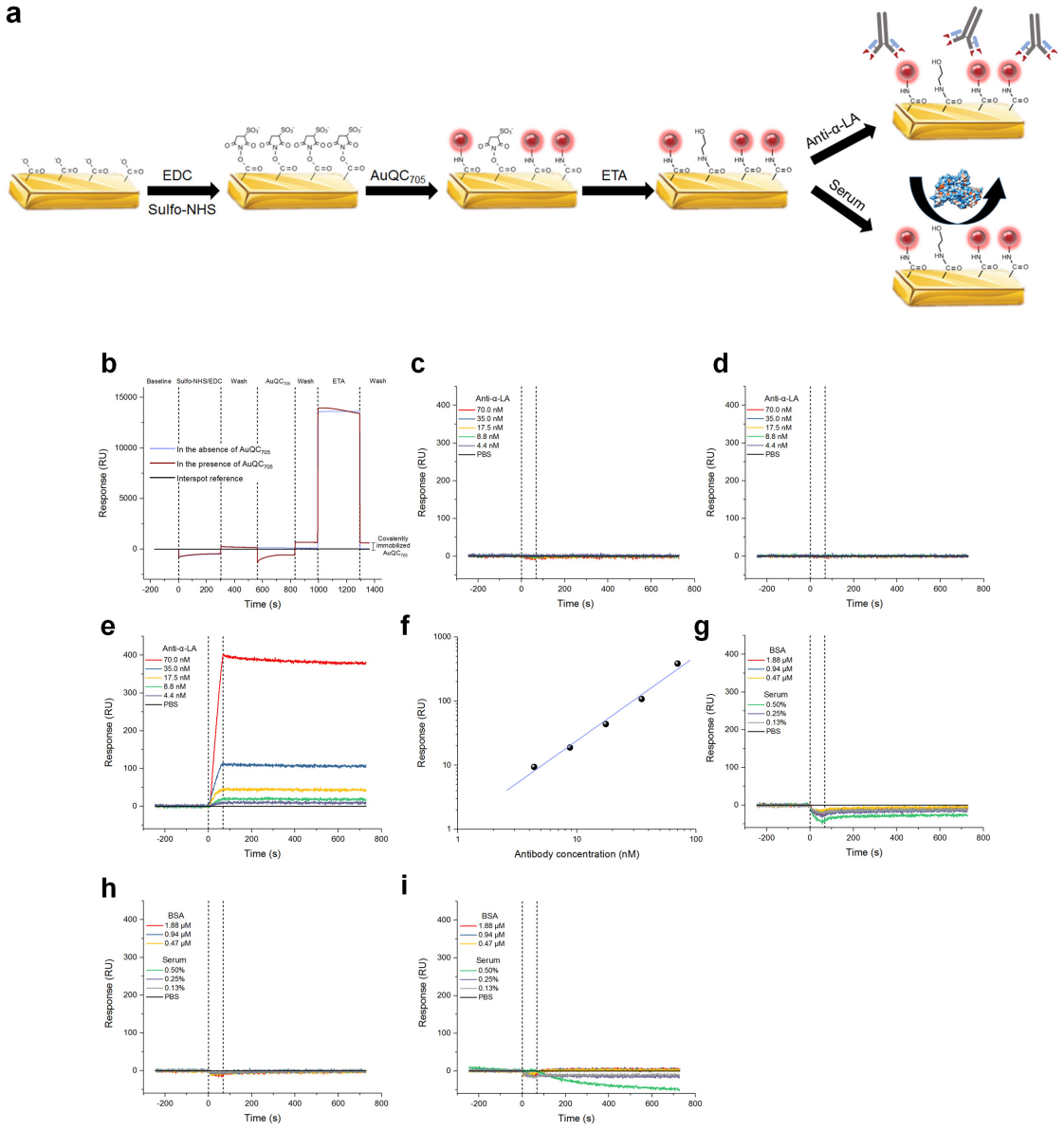

Supplementary Fig. 11 | Interaction of AuQC$_{705}$ with the anti-α-LA antibody and serum. **(a)** Schematic of the surface chemistry for immobilization of AuQC$_{705}$ to investigate serum interaction by surface plasmon resonance (SPR). AuQC$_{705}$ is covalently anchored via its surface amine groups by forming amide bonds with carboxylic acid groups on the alginate-modified gold surface using sulfo-NHS/1-ethyl-3-(3-dimethylaminopropyl)carbodiimide (EDC) chemistry. Unreacted NHS groups are blocked by ethanolamine (ETA) before monitoring interaction with anti-α-LA antibody, bovine serum albumin (BSA) or mouse serum. **(b)** SPR profiles for steps of surface chemistry and immobilization of AuQC$_{705}$. AuQC$_{705}$ was successfully immobilized through covalent bonds, as clearly observed by the positive SPR signals after the final washing step. Both the channel with identical surface chemistry in the absence of AuQC$_{705}$ and the interlane control do not exhibit an increment in SPR signals. Serial concentrations of anti-α-LA antibody do not display SPR responses **(c)** in the absence of AuQC$_{705}$ or **(d)** in the interlane, but present **(e-f)** a linear concentration-dependent specific response in the presence of AuQC$_{705}$. In contrast, neither BSA nor mouse serum can induce any positive SPR responses in the channel without AuQC$_{705}$ **(g)**, the interlane **(h)** or the channel with AuQC$_{705}$ **(i)**. AuQC$_{705}$ therefore preserves the specific binding affinity for anti-α-LA antibody while minimally interacting with serum.

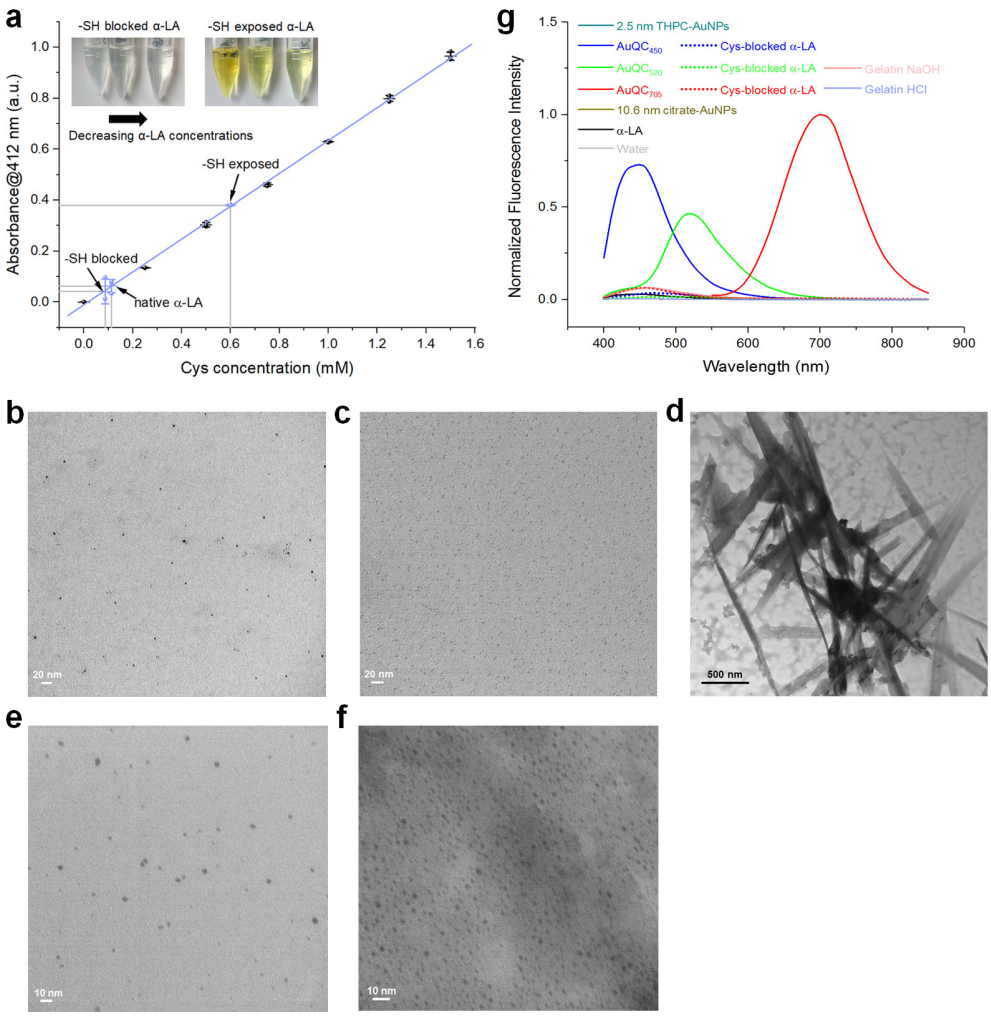

Supplementary Fig. 12 | The effect of Au-S bonds on fluorescence of AuQCs.
(a) Determination of sulfhydryl groups by Ellman's assay. Standards of cysteine at 0, 0.25, 0.5, 0.75, 1.0, 1.25 and 1.5 mM were linearly fitted. The thiols in 71 μM of native, -SH exposed or blocked α-LA were determined by the calibration curve. A theoretical 0.57 mM Cys in -SH exposed α-LA was found to be 0.60±0.03 mM, while only 0.09±0.10 and 0.11±0.07 mM were found for –SH blocked or native α-LA respectively. Inset shows photographs of –SH blocked and exposed α-LA (2.82, 0.57 and 0.28 mM sulfhydryls) after reaction, demonstrating free thiols were efficiently blocked. TEM images of AuQCs synthesized using thiol-blocked α-LA at the same optimal conditions as using native α-LA for **(b)** $AuQC_{450}$, **(c)** $AuQC_{520}$ and **(d)** $AuQC_{705}$. As-synthesized AuNPs retained ultrasmall sizes under conditions for $AuQC_{450}$ and $AuQC_{520}$ but self-assembled into Au-α-LA nanotubes, a nanostructure formed by α-LA only at high concentrations in the presence of Ca^{2+}[1]. **(e-f)** TEM images of ultrasmall AuNPs synthesized using porcine gelatin without Cys under **(e)** acidic and **(f)** alkaline conditions. 5 mg/mL type A gelatin derived from collagen (acid-cured porcine skin ~300 g Bloom, Sigma) was used to replace α-LA for synthesis, due to its relatively low aqueous solubility. Although detailed amino acid composition of heterogeneous gelatin has not been clearly elucidated, gelatin from skin sources contains <0.1% Cys of total residues[2-4]. **(g)** Fluorescence spectra of AuNPs and AuQCs. Native α-LA only has a weak protein intrinsic blue fluorescence. 2.5 nm and 10.6 nm AuNPs barely exhibit any fluorescence. With Cys in α-LA blocked, ultrasmall AuNPs synthesized under the same conditions exhibited much weaker fluorescence. AuNPs synthesized with gelatin at both low and high pH only resulted in weak blue fluorescence, despite their ultrasmall morphologies similar to AuQCs. Excitation wavelength: 360 nm.

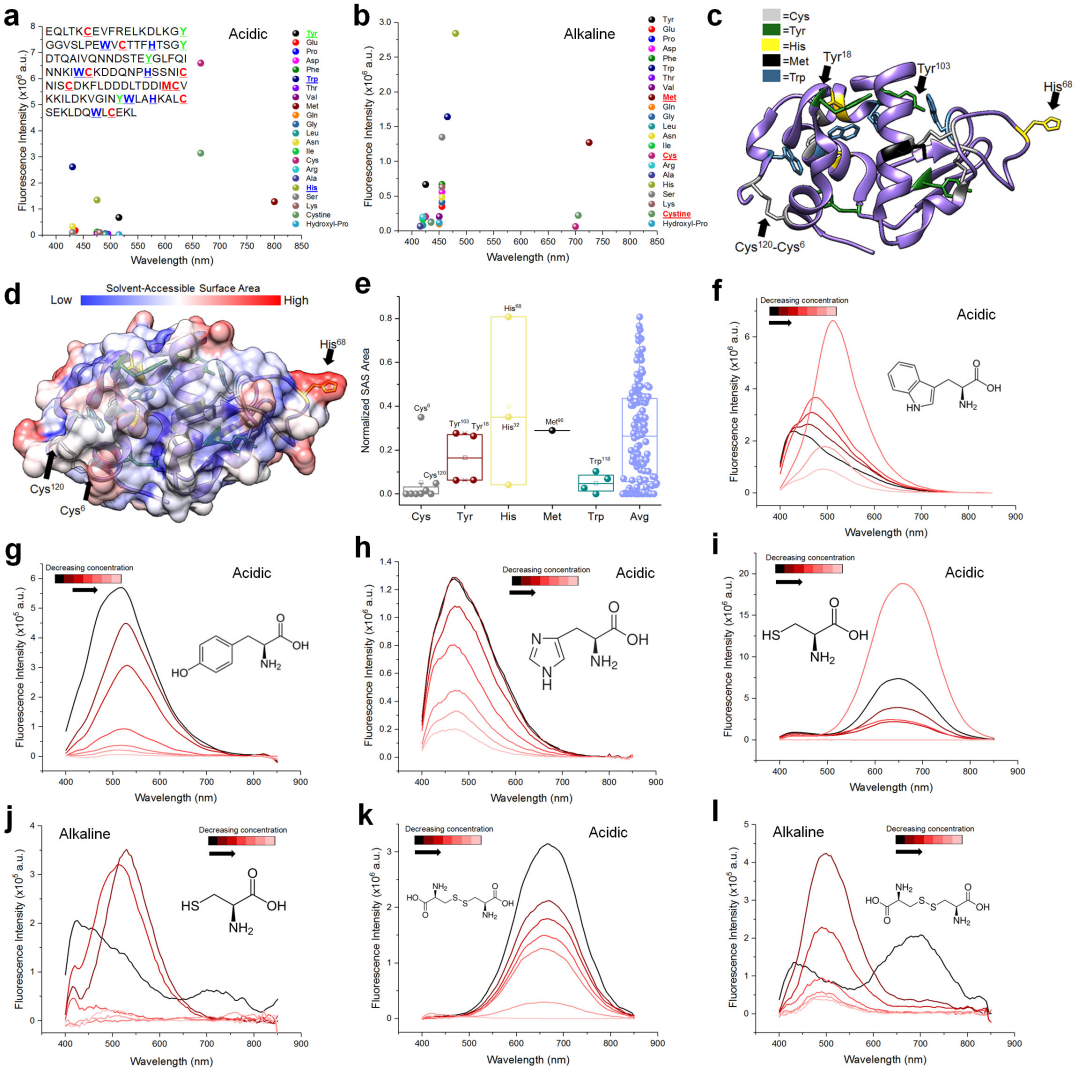

Supplementary Fig. 13 | Effects of individual amino acids on fluorescence of AuQCs. **(a-b)** Scatter plots of fluorescence peak intensities and wavelengths of AuNPs synthesized with all 20 amino acids present in the 123 residues (sequence as inset) of the α-LA primary structure as well as cystine and hydroxylproline under **(a)** acidic and **(b)** alkaline conditions. Hydroxylation of Pro did not result in strong fluorescence. A number of amino acids such as His, Trp and Ser induce the minor blue fluorescence peak in $AuQC_{705}$ (Fig. 2a). **(c)** Amino acids identified to be involved in the major fluorescence of AuQCs including Cys, Tyr, His, Trp and Met. Their positions in the structure of α-LA (PDB ID: 1F6R) are colour-coded. **(d)** Surface map of solvent-accessible surface (SAS) area for amino acids in α-LA. **(e)** Calculated normalized SAS area of amino acid residues in α-LA[5]. **(f-l)** Synthesis at various concentrations of 0.31, 0.63, 1.25, 2.5, 5.0, 10.0 and 20.0 mg/mL for Trp, Tyr, His, Cys and $(Cys)_2$ in (**f-i** and **k**) acidic and (**j** and **l**) alkaline conditions.

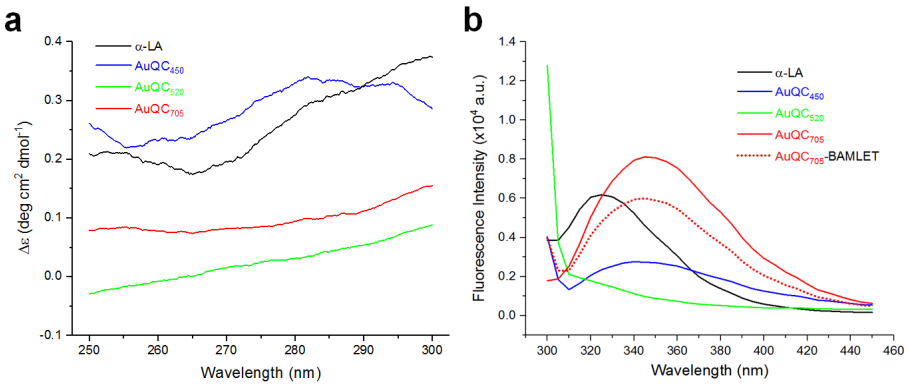

Supplementary Fig. 14 | Structural characterization of AuQCs. (a) Near-UV circular dichroism (CD) and **(b)** intrinsic tryptophan fluorescence spectra of α-LA and AuQCs. Native α-LA showed an emission peak at 327 nm, typical for Trp residues buried in hydrophobic protein core, consistent with SAS area of Trp in Supplementary Fig. 13e. Trp peaks shifted bathochromically indicating unfolding[6], while the weak Trp fluorescence of $AuQC_{520}$ suggests strong quenching and low α-LA abundance. Note that Trp fluorescence intensity of $AuQC_{705}$ increases owing to a more hydrophobic microenvironment and weaker quenching from side chains and peptide bonds. This demonstrates that partial refolding might occur after unfolding, induced by nucleation of NPs. Trp-selective excitation wavelength: 295 nm.

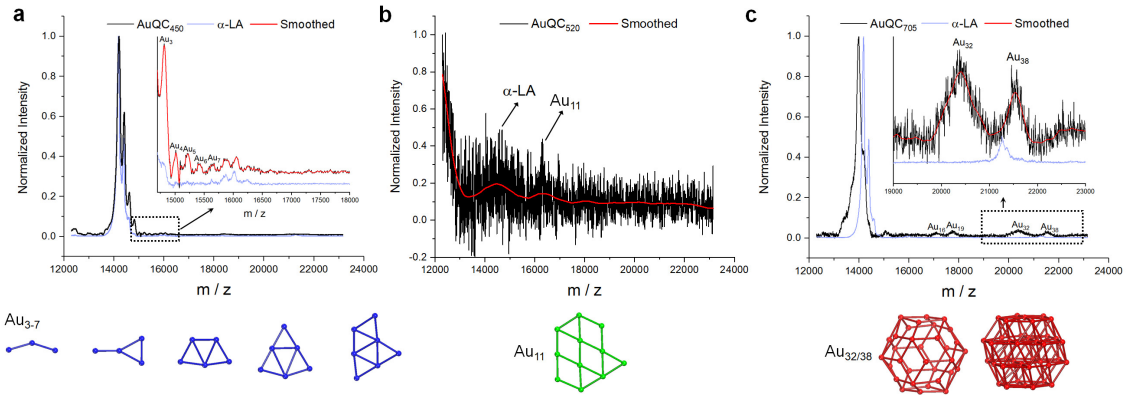

Supplementary Fig. 15 | Matrix-assisted laser desorption/ionization time-of-flight mass spectra (**MALDI-TOF-MS**) of **(a)** $AuQC_{450}$, **(b)** $AuQC_{520}$ and **(c)** $AuQC_{705}$. Native α-LA was included as a reference for **a** and **c**. Data were normalized and weighted adjacent-averaging was used to smooth the original data for better peak observations. Boxed area shows magnification. Besides the parent protein peak that serves as stabilizing ligands, major well-defined Au molecular structures contributing to fluorescence were identified by a set of fragmented peaks as Au_{3-7} in $AuQC_{450}$, Au_{11} in $AuQC_{520}$ and $Au_{32/38}$ complex in $AuQC_{705}$. The low-intensity parent protein MALDI peak of $AuQC_{520}$ is ascribed to the extremely low abundance of α-LA, consistent with its small hydrodynamic size (Fig. 2b). The irreversible minor downshift of parent protein peak in $AuQC_{705}$ is due to break of disulfide bonds and deamidation from hydrolysis of peptide bonds during the synthesis at alkaline pH[7]. The $Au_{32/38}$ complex is likely to be derived from dimerization of the $Au_{16/19}$ complex that coexists in $AuQC_{705}$. In the meantime, the α-LA parent protein peaks in $AuQC_{450}$ and $AuQC_{705}$ manifest the existence of stabilizing α-LA that can contribute to formation of BAMLET (bovine α-LA made lethal to tumor cells) anti-cancer lipoprotein complex in the presence of OA. Schematic of AuQCs is shown below the graphs (not the actual orientations).

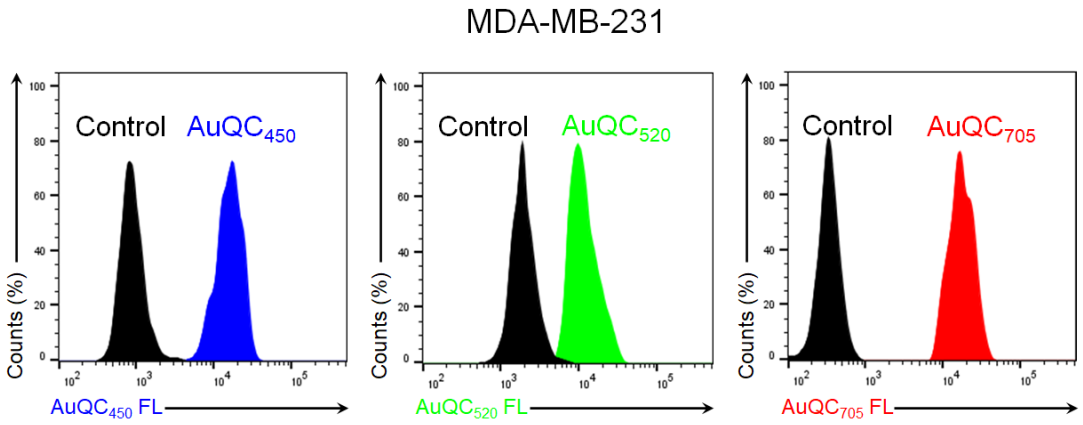

Supplementary Fig. 16 | Flow cytometry for uptakes of AuQCs. All AuQCs were observed to have uptakes in MDA-MB-231 cancer cells.

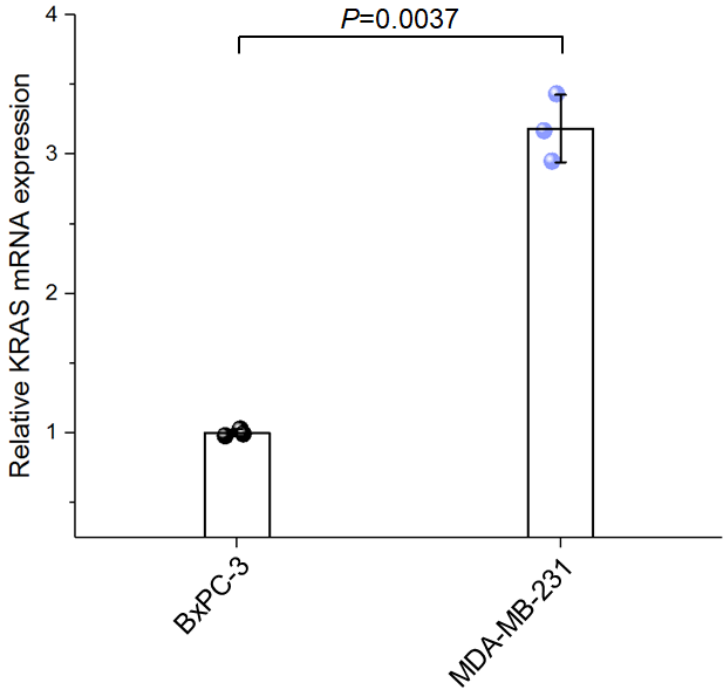

Supplementary Fig. 17 | KRAS mRNA expression of human tumour cells. Expressions relative to the β-actin (ACTB) control were measured by quantitative PCR (qPCR) with reverse transcription. KRAS status of human pancreatic cancer cell line BxPC-3 and human breast cancer cell line MDA-MB-231 was verified at the Cancer Cell Line Encyclopedia (www.broadinstitute.org/ccle). While BxPC-3 expresses wild-type KRAS, MDA-MB-231 is a KRAS mutant. The qPCR confirmed the high KRAS mRNA expression level in MDA-MB-231 cells compared to BxPC-3 (n=3 biologically independent samples).

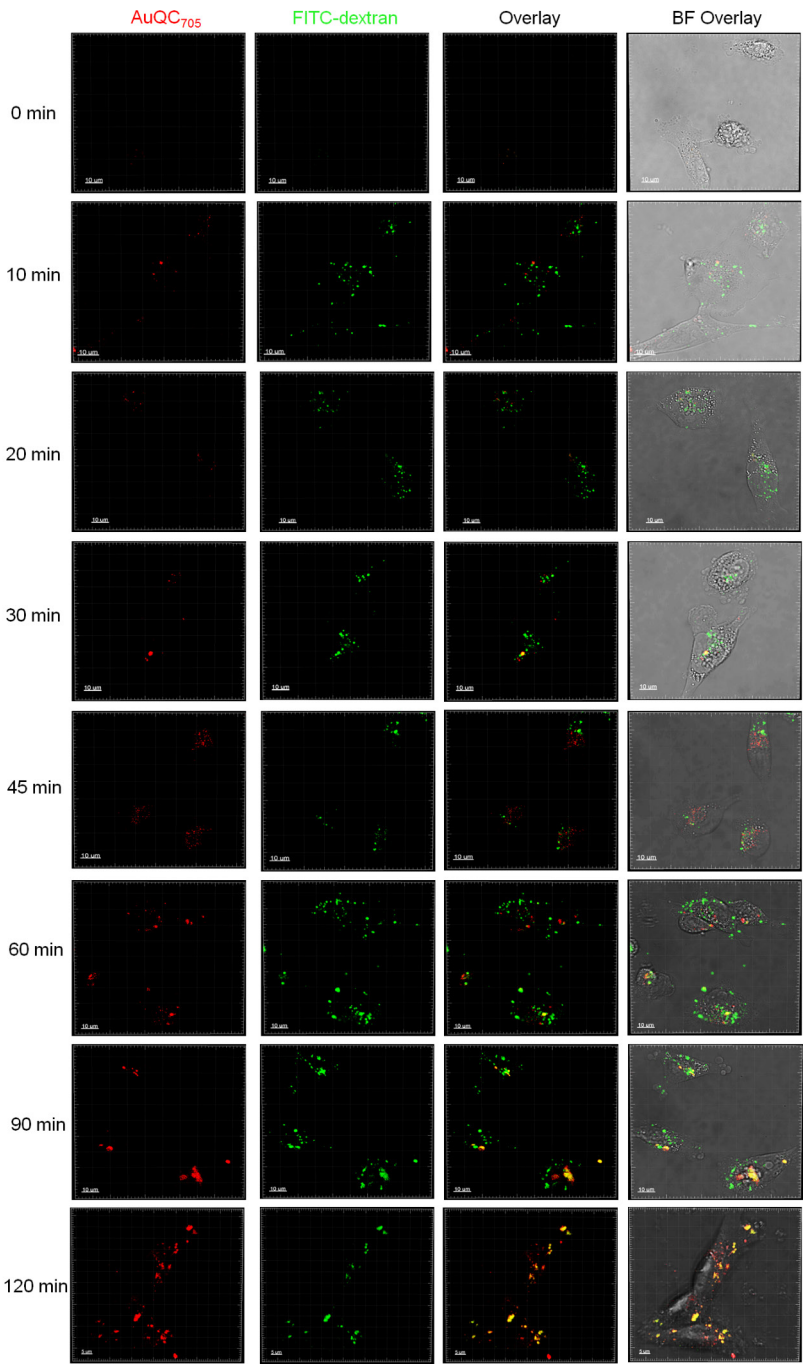

Supplementary Fig. 18 | Time-course macropinocytosis of AuQC$_{705}$. MDA-MB-231 cancer cells were tracked by a well-established fluid-phase macropinocytosis marker fluorescein isothiocyanate-labeled high-molecular-weight dextran (FITC-dextran), with a hydrodynamic size of 3.3 nm and a molecular mass of ~20 kDa similar to AuQC$_{705}$. While both AuQC$_{705}$ (red) and FITC-dextran (green) were accumulated in puncta-like subcellular compartments of macropinocytic origin, linear, flexible and hyperpermeable FITC-dextran with a larger sieving coefficient was taken up faster across membranes than spherical compact AuQC$_{705}$ with lower molecular deformability, even at equivalent molecular masses[8]. While partial colocalization (yellow) was observed initially, a high extent was observed at 2 h.

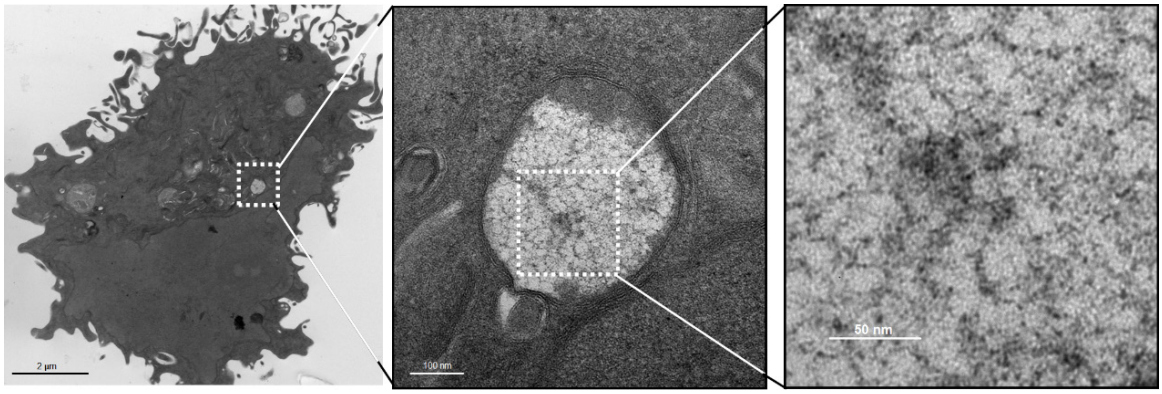

Supplementary Fig. 19 | Ultrastructure analysis of MDA-MB-231 cells. Cells were incubated with $AuQC_{705}$ for 2 h. A small-sized and regularly-shaped lysosome vesicle away from plasma membrane can be seen. $AuQC_{705}$ in the cargo is retained in ultrasmall size which reserves its fluorescence.

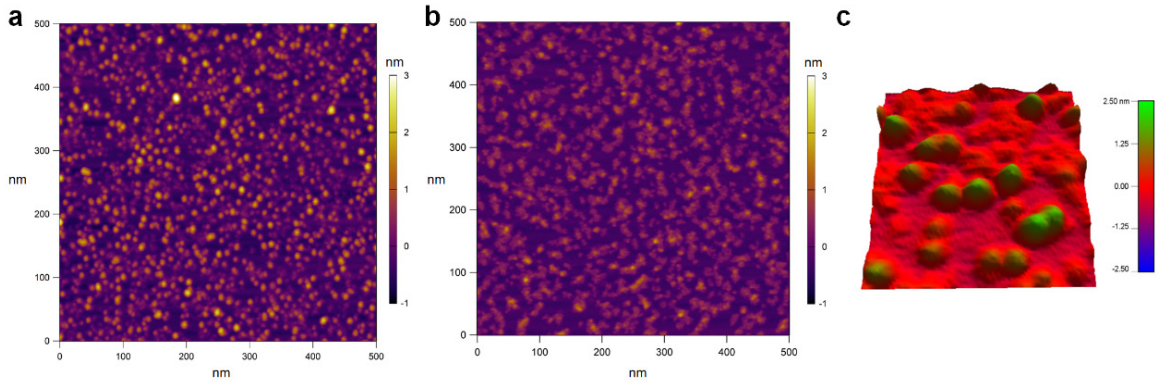

Supplementary Fig. 20 | Atomic force microscopy (AFM) characterization of $AuQC_{705}$. **(a)** A low-resolution topological AFM image of $AuQC_{705}$ under tapping mode. A highly monodispersed globular population of $AuQC_{705}$ with an average height profile of 1.8±0.4 nm is evenly distributed in the α-LA matrix observed as the obscure irregular surrounding area with a much smaller height. **(b)** A low-resolution AFM image of α-LA showing an amorphous irregularly-shaped morphology distinct from $AuQC_{705}$. **(c)** A high-resolution three-dimentional (3D) topograph showing $AuQC_{705}$ embedded in the α-LA matrix.

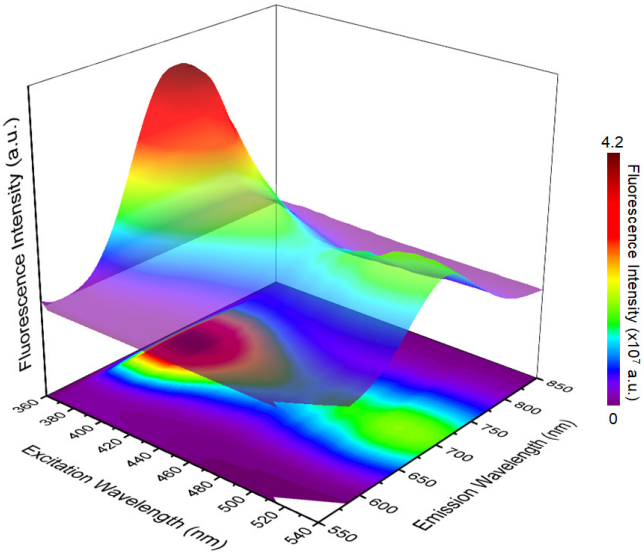

Supplementary Fig. 21 | Photoluminescence excitation (PLE) spectrum of $AuQC_{705}$. NIR emission near 700 nm can be selectively excited in both UV and visible regions. Relative fluorescence intensity is intuitively displayed by the top 3D trajectory.

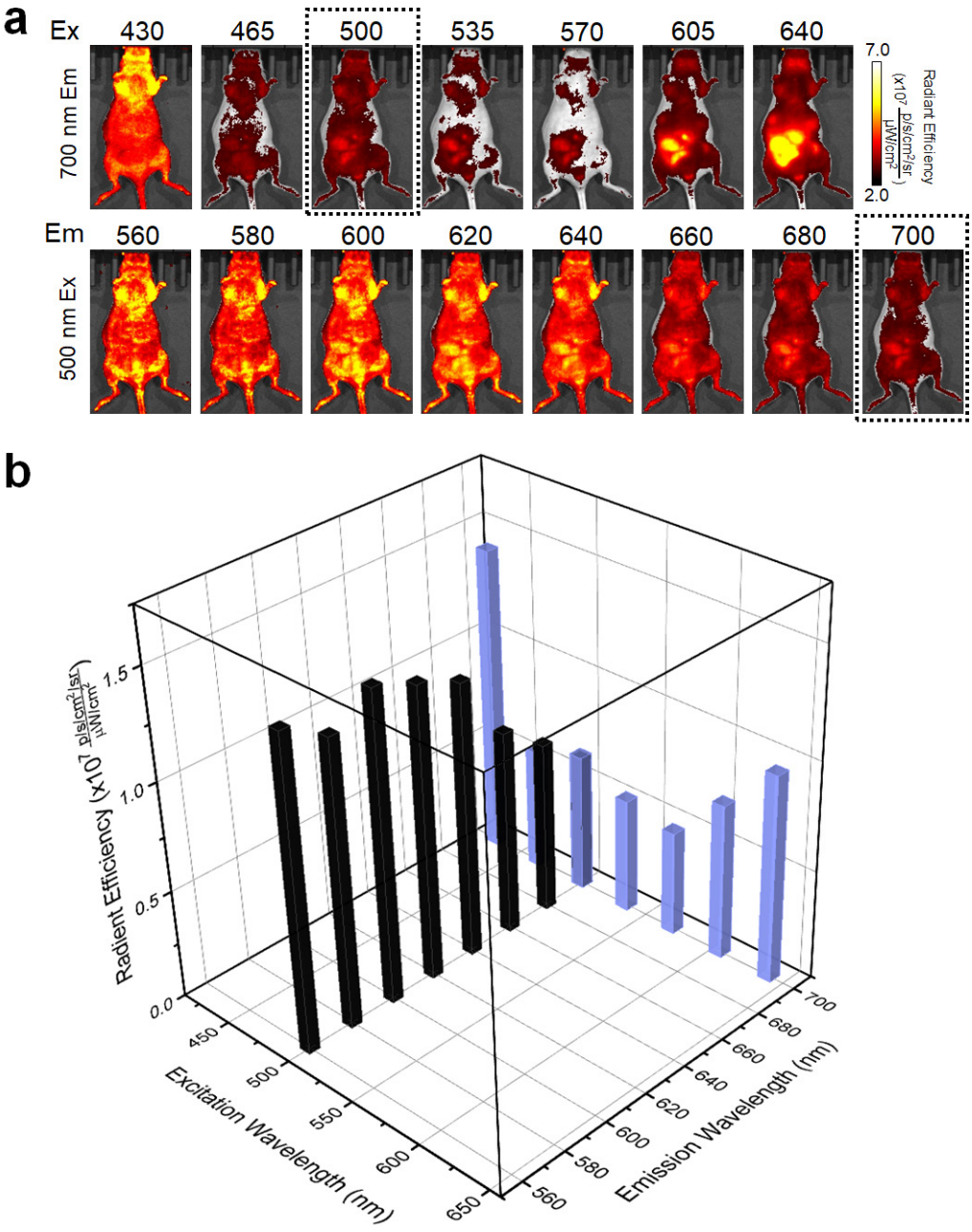

Supplementary Fig. 22 | Whole-body autofluorescence investigation of a J:NU mouse. **(a)** Autofluorescence imaging at 700 nm emission excited by different wavelengths (top) or at different emission wavelengths excited by 500 nm (bottom). Mice were kept on low-fluorescence imaging diet 5V75 (LabDiet Inc.) for 10 days before imaging. The boxed imaging condition is used for $AuQC_{705}$. **(b)** Quantification of whole-body averaged autofluorescence. Autofluorescence at 700 nm emission is low in the range of 465-570 nm (570 nm being the lowest), while at 500 nm excitation, larger Stokes shift endows lower overall autofluorescence, especially near the 2nd, 3rd thoracic and 4th abdominal mammary fat pads involved in breast cancer imaging.

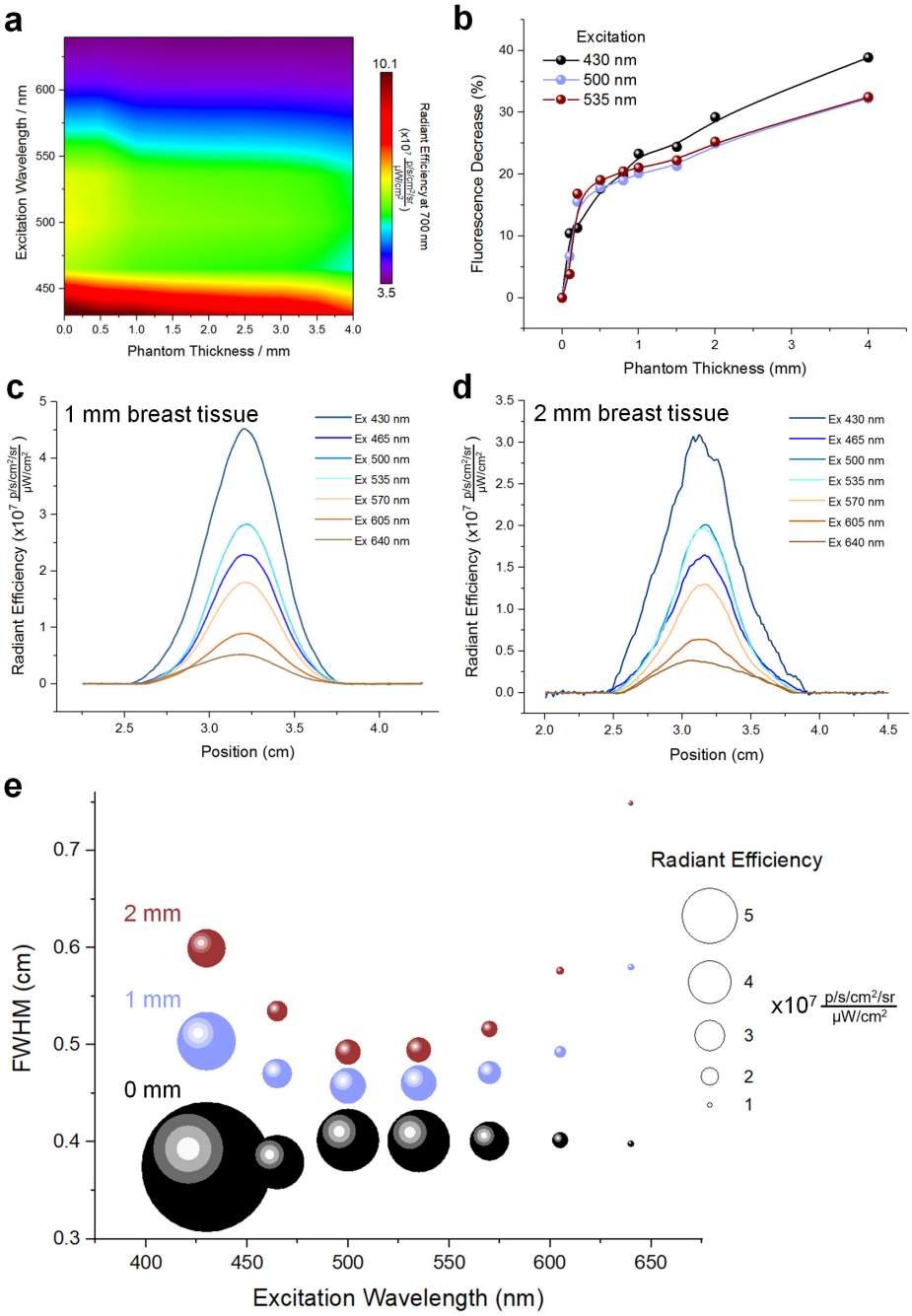

Supplementary Fig. 23 | Fluorescence phantoms of AuQC$_{705}$. (a) PLE spectrum of AuQC$_{705}$ in a quartz tube as a function of the thickness of vibratome-cut agarose phantoms (4% w/w). **(b)** Fluorescence intensity decrease of AuQC$_{705}$ as a function of phantom thickness at excitation wavelengths of 430, 500 and 535 nm. Despite the initial strongest fluorescence at 430 nm excitation, it decreased more with increasing phantom thickness. **(c-d)** Cross-sectional fluorescence intensity profiles of AuQC$_{705}$ at 700 nm in a quartz tube with chicken breast tissue sections at **(c)** 1 mm and **(d)** 2 mm as a function of excitation wavelength. **(e)** Spatial resolution of AuQC$_{705}$ at different thickness of breast tissues as a function of excitation wavelength. The bubble size indicates fluorescence intensity. Both the fluorescence intensity and full width at half maximum (FWHM) dramatically decreased at 430 nm excitation in tissue phantoms compared to longer wavelengths. 500 nm excitation has the optimal FWHM in tissues.

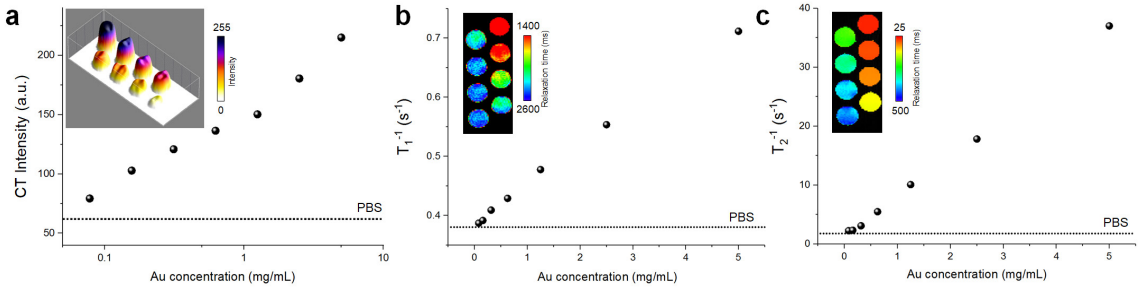

Supplementary Fig. 24 | Computed tomography (CT) and magnetic resonance imaging (MRI) phantoms of AuQC$_{705}$. (a) A linear relationship of averaged CT intensities can be established with $\log_{10}$ concentrations of AuQC$_{705}$. **(b-c)** Linearity of T_1 and T_2 mapping intensities as a function of concentrations. Dotted lines in all figures indicate PBS control. Corresponding phantom images are shown as insets.

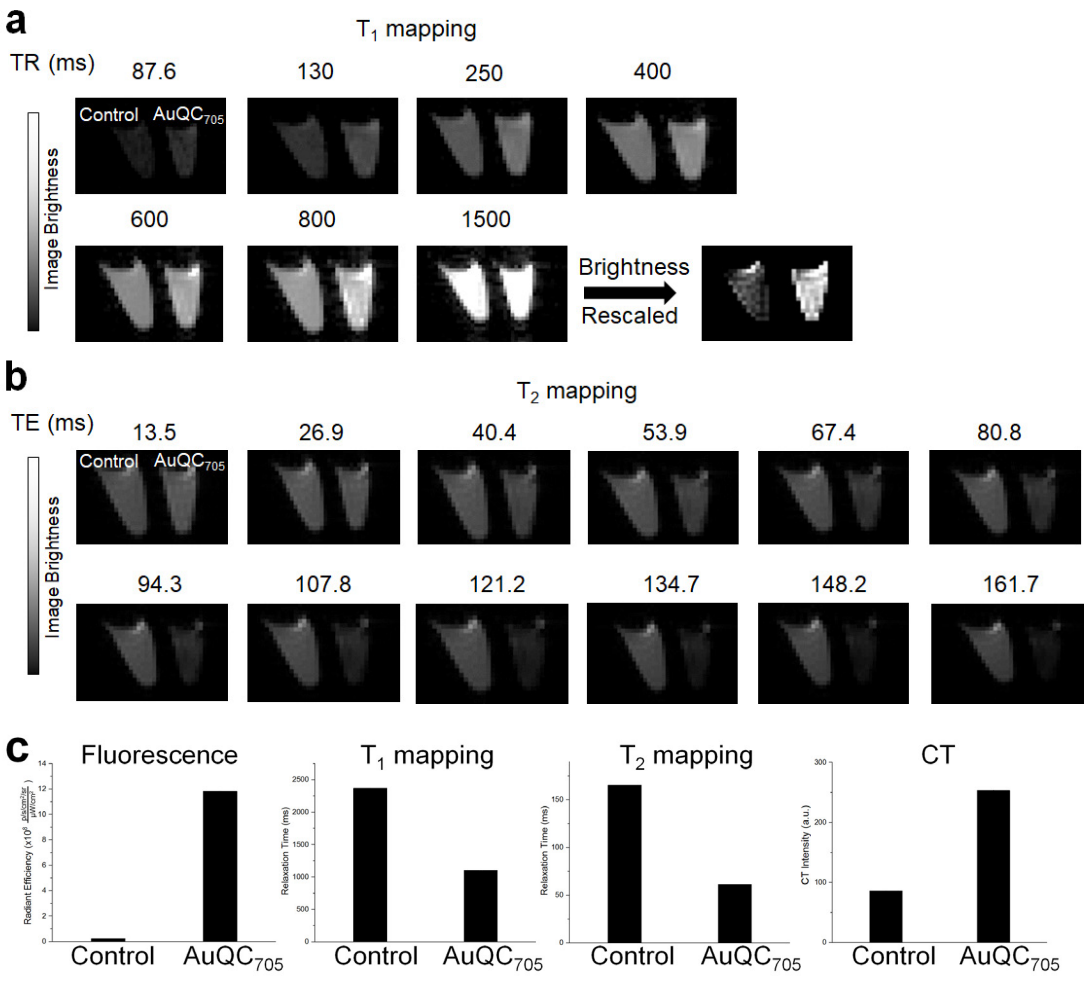

Supplementary Fig. 25 | T_1 and T_2 MRI mapping images of MDA-MB-231 cell phantoms with AuQC$_{705}$ uptake. (a) T_1 scan was taken at 19.3 ms echo time (TE) with different repetition time (TR). **(b)** T_2 scan was obtained at 2000 ms TR with varying TE. **(c)** Corresponding averaged phantom signal intensities by different imaging modalities.

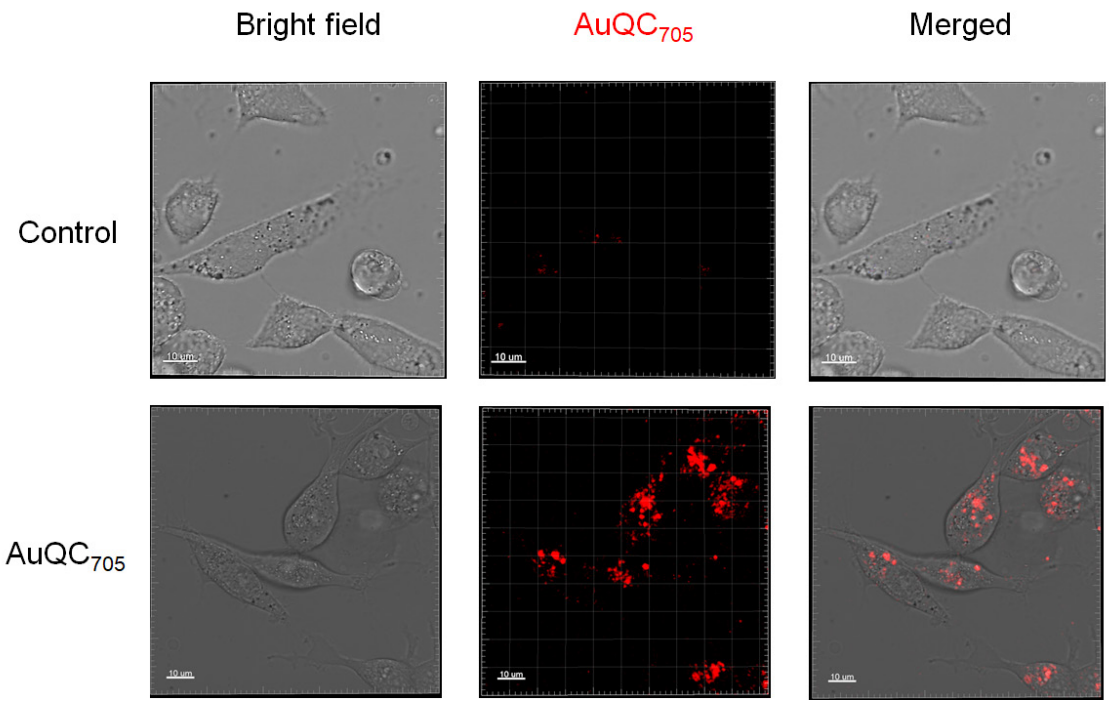

Supplementary Fig. 26 | Confocal fluorescence imaging of MDA-MB-231 cells with $AuQC_{705}$ uptake. In addition to imaging bulk cell phantoms (Fig. 4a), we also imaged individual breast cancer cells using confocal microscopy.

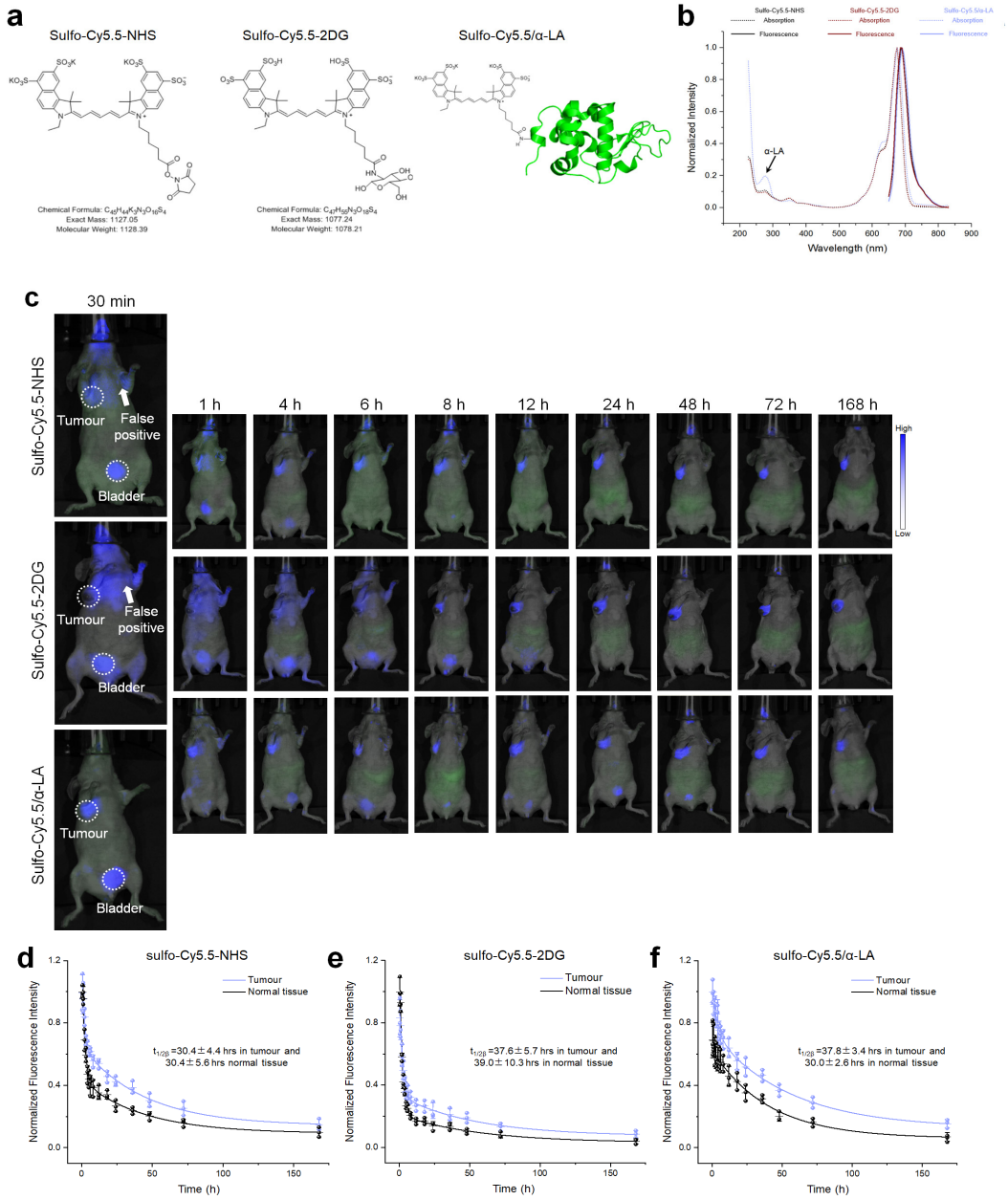

Supplementary Fig. 27 | Comparison of sulfo-Cy5.5-NHS, sulfo-Cy5.5-2DG and sulfo-Cy5.5/α-LA protein-dye complex for non-invasive in vivo fluorescence imaging. (a) chemical structures of NIR-emitting small-molecule sulfo-Cy5.5-NHS and sulfo-Cy5.5-2DG targeting cancer glycolysis, and schematic of sulfo-Cy5.5/α-LA complex. **(b)** Absorption (dotted lines) and fluorescence emission (solid lines) spectra of sulfo-Cy5.5-NHS, sulfo-Cy5.5-2DG and sulfo-Cy5.5/α-LA. While the optical properties of Cy5.5 in absorbance and fluorescence were barely influenced after conjugation to 2DG and α-LA by NHS, an absorbance peak at 280 nm indicative of α-LA can be observed for sulfo-Cy5.5/α-LA. The number of Cy5.5 per α-LA molecule was quantified to be ~1. **(c)** Noninvasive fluorescence images of MDA-MB-231 human breast cancer xenograft mice after intravenous (i.v.) injection. **(d-f)** Time-fluorescence intensity curves for tumours and normal tissues obtained from fluorescence imaging after injection of **(d)** sulfo-Cy5.5-NHS, **(e)** sulfo-Cy5.5-2DG and **(f)** sulfo-Cy5.5/α-LA. Curves were fitted with two-compartment pharmacokinetic models (sulfo-Cy5.5-NHS: R^2=0.991 and 0.993 for tumour and normal tissues; sulfo-Cy5.5-2DG: R^2=0.995 and 0.993 for tumour and normal tissues; sulfo-Cy5.5/α-LA: R^2=0.998 and 0.985 for tumour and normal tissues). The retention half-lives in MDA-MB-231 tumours are shown.

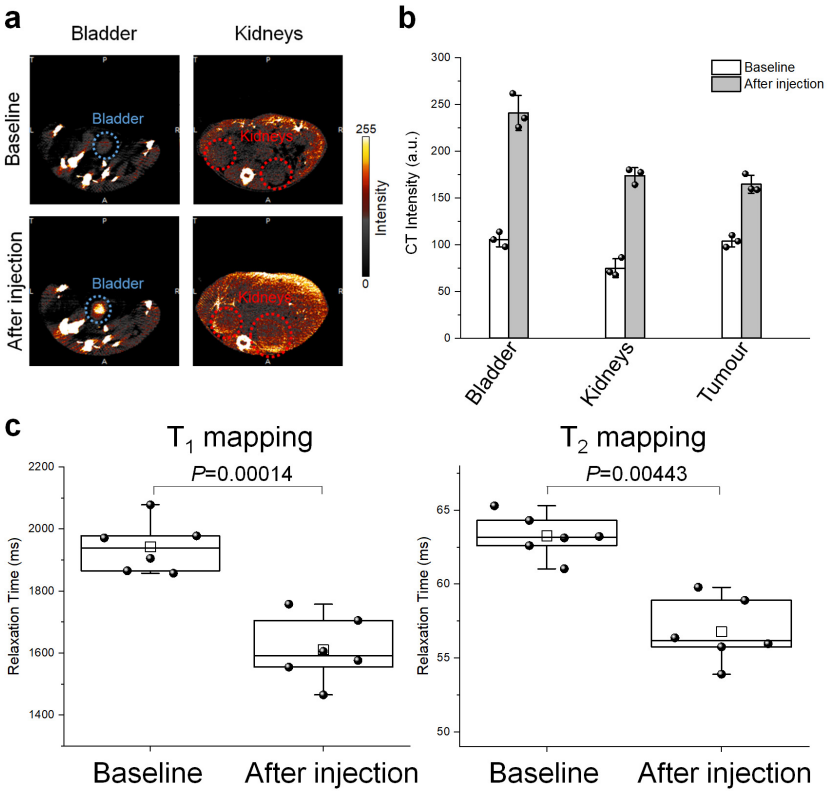

Supplementary Fig. 28 | In vivo imaging of AuQC$_{705}$ by different imaging modalities. (a) Micro-CT images of bladder and kidneys of J:NU mice bearing MDA-MB-231 tumours after i.v. injection of AuQC$_{705}$. Kidneys and the bladder can be clearly identified 1 h after injection. **(b)** Quantification for averaged CT signals of tumour, bladder and kidneys (n=3 slices). **(c)** Quantification for relaxation times of MRI slices (n=6 slices). The box represents 50% interquantile range. The middle line dividing the box indicates the median, while the empty square □ indicates the mean. Min and Max are marked by the upper and lower lines.

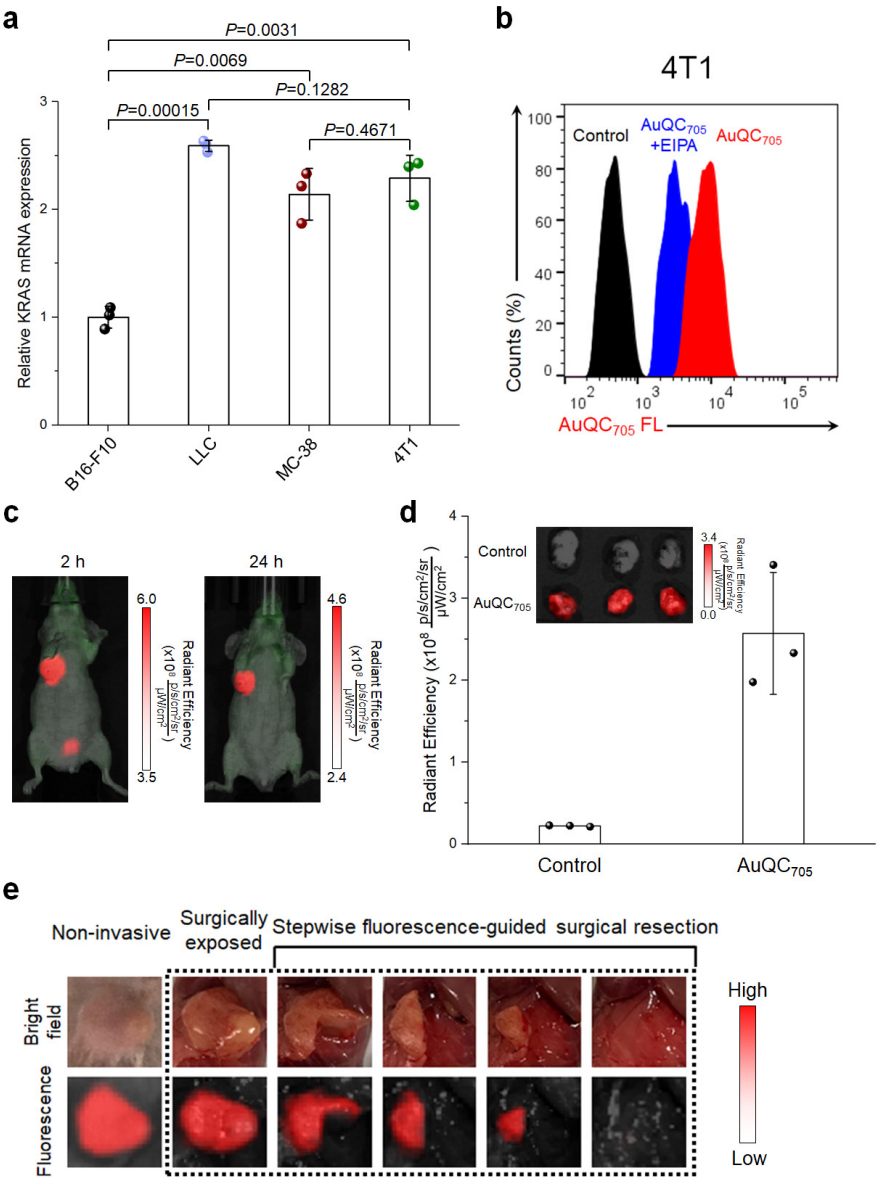

Supplementary Fig. 29 | Imaging and intraoperative surgical guidance of murine breast cancer with AuQC$_{705}$. (a) KRAS mRNA expression profile of 4T1 mouse breast cancer cells relative to ACTB by qPCR with reverse transcription. KRAS wild-type mouse melanoma cell line B16-F10 and KRAS mutants, LLC mouse lung cancer cell line and MC-38 mouse colon cancer cell line, were included as negative and positive controls respectively[9]. The oncogenic RAS signaling pathway has been demonstrated to be activated in 4T1[10]. Here we show that 4T1 has an elevated KRAS mRNA expression close to LLC and MC-38 cells (n=3 biologically independent samples). **(b)** The uptake of AuQC$_{705}$ in 4T1 mouse breast cancer cells can be inhibited by 5-(*N*-ethyl-*N*-isopropyl)-amiloride (EIPA), suggesting macropinocytosis is a major intracellular trafficking pathway. **(c)** Noninvasive in vivo fluorescence imaging of mice bearing 4T1 murine breast tumours after i.v. injection of AuQC$_{705}$. **(d)** Ex vivo fluorescence imaging of 4T1 tumours 24 h after injection of AuQC$_{705}$. **(e)** NIR fluorescence image-guided intraoperative surgeries of 4T1 tumours using AuQC$_{705}$ 24 h after injection. The tumour near the upper mammary fat pad was surgically exposed and stepwise resected under guidance of the specific signals of AuQC$_{705}$. Complete removal was validated by the absence of fluorescence on the resection bed.

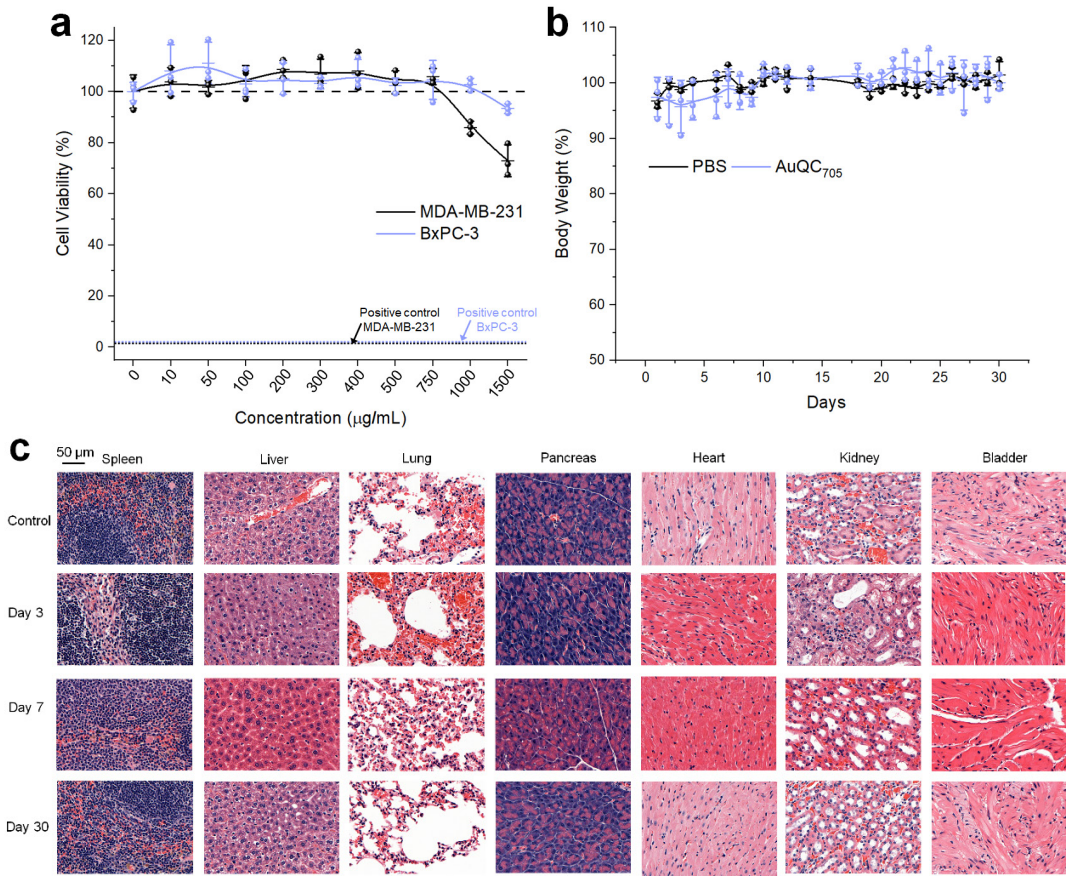

Supplementary Fig. 30 | Toxicological evaluation of $AuQC_{705}$. (a) In vitro cytotoxicity evaluation of $AuQC_{705}$ in MDA-MB-231 breast and BxPC-3 pancreatic cancer cell lines after 24 h incubation using 3-(4,5-dimethylthiazol-2-yl)-2,5-diphenyltetrazolium bromide (MTT) assay. 1 mM SDS was used as positive controls. **(b)** Body weight of BALB/cJ mice (n=3 biologically independent animals) after i.v. injection of $AuQC_{705}$ (187.5 mg Au/kg). **(c)** Histopathological evaluation by haematoxylin and eosin (H&E) staining for different organs harvested after i.v. injection of $AuQC_{705}$. Control mice were injected with PBS.

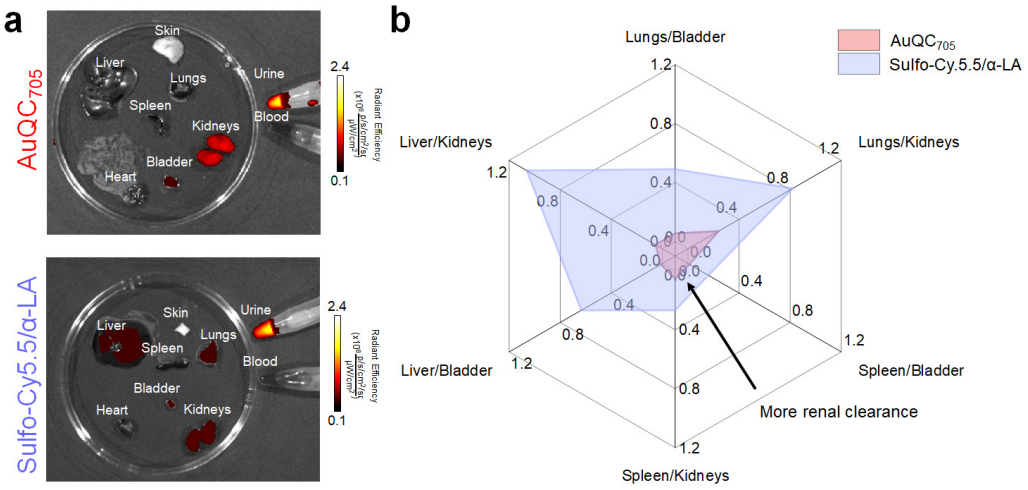

Supplementary Fig. 31 | AuQC$_{705}$ is more renal clearable than native α-LA. (a) Ex vivo fluorescence images of major organs dissected from BALB/cJ wild-type mice 6 h after injection of AuQC$_{705}$ and sulfo-Cy5.5/α-LA. Urine was collected at the time of sacrifice. **(b)** Signal ratios of averaged fluorescence intensities of liver, spleen and lung to kidneys and bladder were calculated.

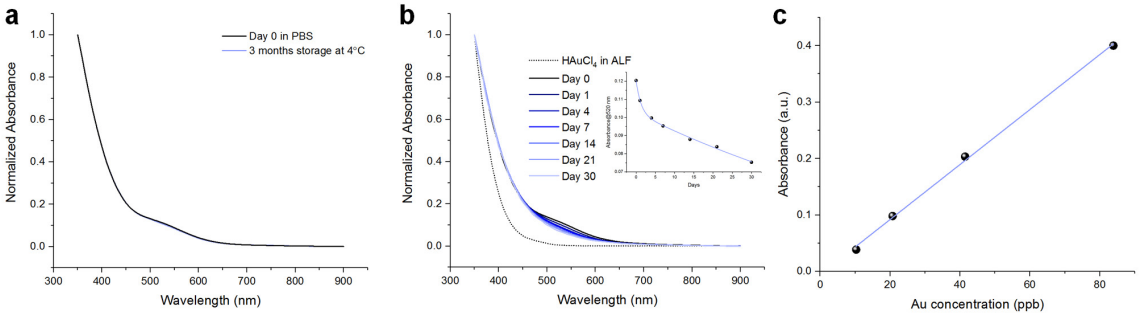

Supplementary Fig. 32 | In vitro degradability of AuQC$_{705}$. (a) UV-vis spectrum of AuQC$_{705}$ after 3 months of storage in PBS at 4°C without observation of obvious spectral changes showing high stability. **(b)** Time-course UV-vis absorption spectra of AuQC$_{705}$ in artificial lysosomal fluid (ALF) at 37°C mimicking lysosomal degradation conditions in vitro. Inset shows that the characteristic peak of AuQC$_{705}$ near 520 nm gradually diminished with time. **(c)** Calibration curve of Au standards using atomic absorption spectroscopy (AAS) with a lower linearity of dynamic working range as low as 10 ppb. It has been previously reported that AuNPs via endocytosis can be degraded into $Au^{1+/3+}$ ions under lysosomal conditions[11]. To further verify degradability, we lysed MDA-MB-231 cells which were harvested after 24, 48 and 72 h incubation with 750 μg/mL AuQC$_{705}$, using CelLytic^{TM} M cell lysis buffer (Sigma). These cell lysates along with AuQC$_{705}$ in ALF collected at different time points over a 30-day period were subject to ultracentrifugation with MWCO (molecular weight cutoffs) 3.5 kDa that is sufficient to separate any $Au^{1+/3+}$ ions from degradation[11]. Filtrates were collected and digested with aqua regia for AAS. However, no Au was detected from filtrates of either cell lysates or ALF (data not shown). This may indicate that even if AuQC$_{705}$ is degraded in the lysosomes or ALF, but the degradation product $Au^{1+/3+}$ is not released and stays in the protein framework through coordination with amino acids of α-LA, in a way similar to the complex formation during synthesis (but not reduced into metallic Au). This may also explain why the cytotoxicity of AuQCs is relatively low. However, these in vitro data cannot demonstrate degradation of AuQC$_{705}$ and we next investigated its fates in vivo.

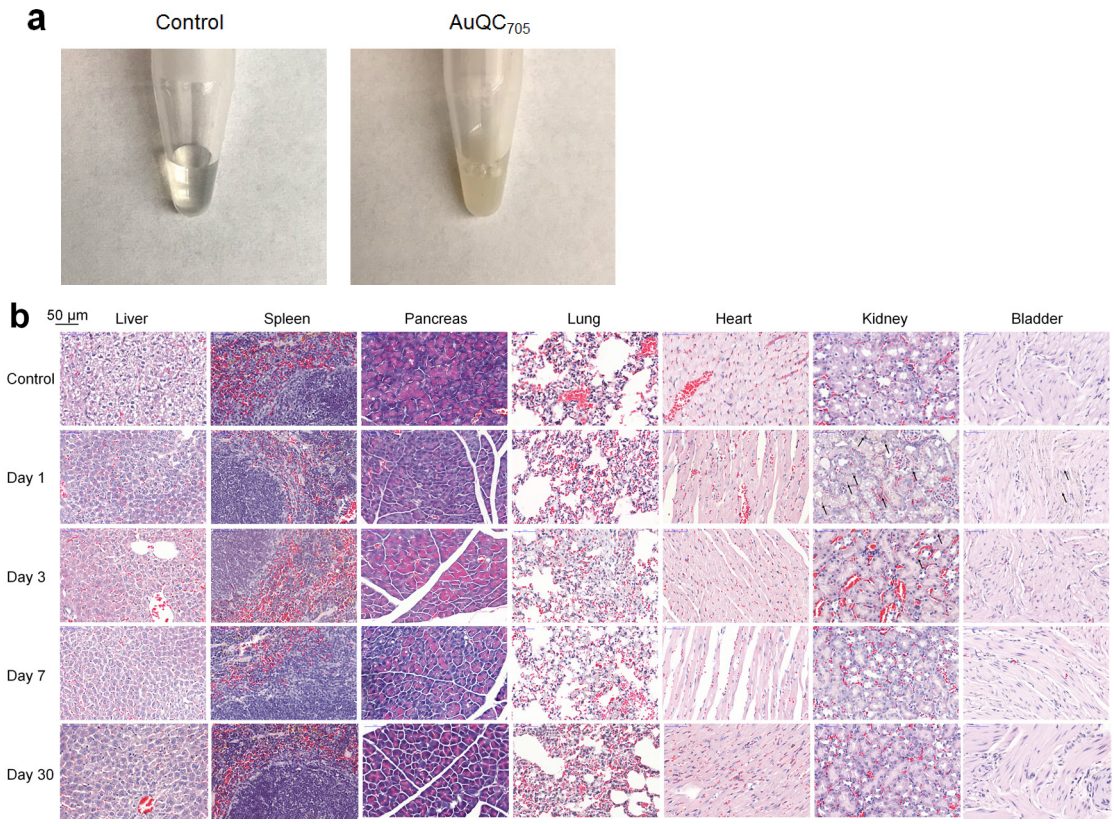

Supplementary Fig. 33 | $AuQC_{705}$ has minimal long-term retentions in vivo in major organs. **(a)** Photographs showing $AuQC_{705}$-mediated catalysis for silver deposition and growth. $AuQC_{705}$ acts as the nucleation centre and catalyzes the reduction of Ag^+ ions into metallic silver in brown or black precipitates around the ultrasmall nanoparticles[12]. **(b)** Silver staining of major organs histologically embedded and sectioned from BALB/cJ mice after i.v. injection of $AuQC_{705}$. Control mice were injected with PBS. The spleen, pancreas and lungs are observed with relatively high native background staining, but $AuQC_{705}$ did not further increase the staining, indicating low retention that is consistent with inductively coupled plasma-mass spectrometry (ICP-MS) and ex vivo fluorescence imaging (Supplementary Fig. 34 and Fig. 5h). In contrast, silver-enhanced $AuQC_{705}$ is observed in the kidneys and bladder (black arrows) one day after injection. After three days, only a small proportion of $AuQC_{705}$ can still be detected in the kidneys. The overall staining in all organs is almost at background levels, signifying low organ retentions over prolonged time.

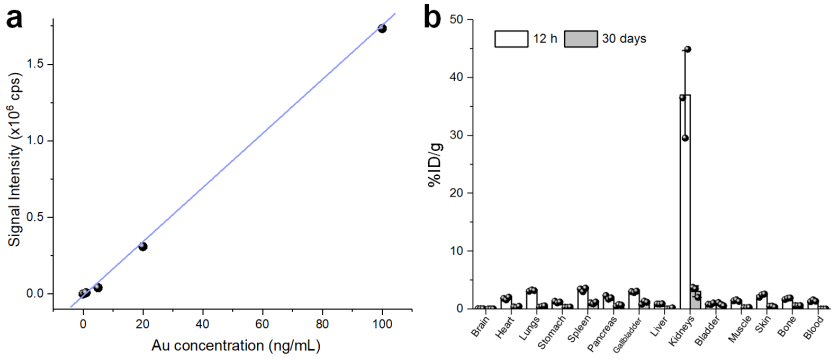

Supplementary Fig. 34 | ICP-MS analysis of long-term body retention of AuQC$_{705}$. (a) ICP-MS standard calibration curve for Au. **(b)** Organs of interest were harvested from J:NU mice (n=3 biologically independent animals) 12 h and 30 days after injection of AuQC$_{705}$ for quantification of Au by ICP-MS. The Au content in all organs was found to decrease significantly after 30 days, suggesting minimal long-term retention.

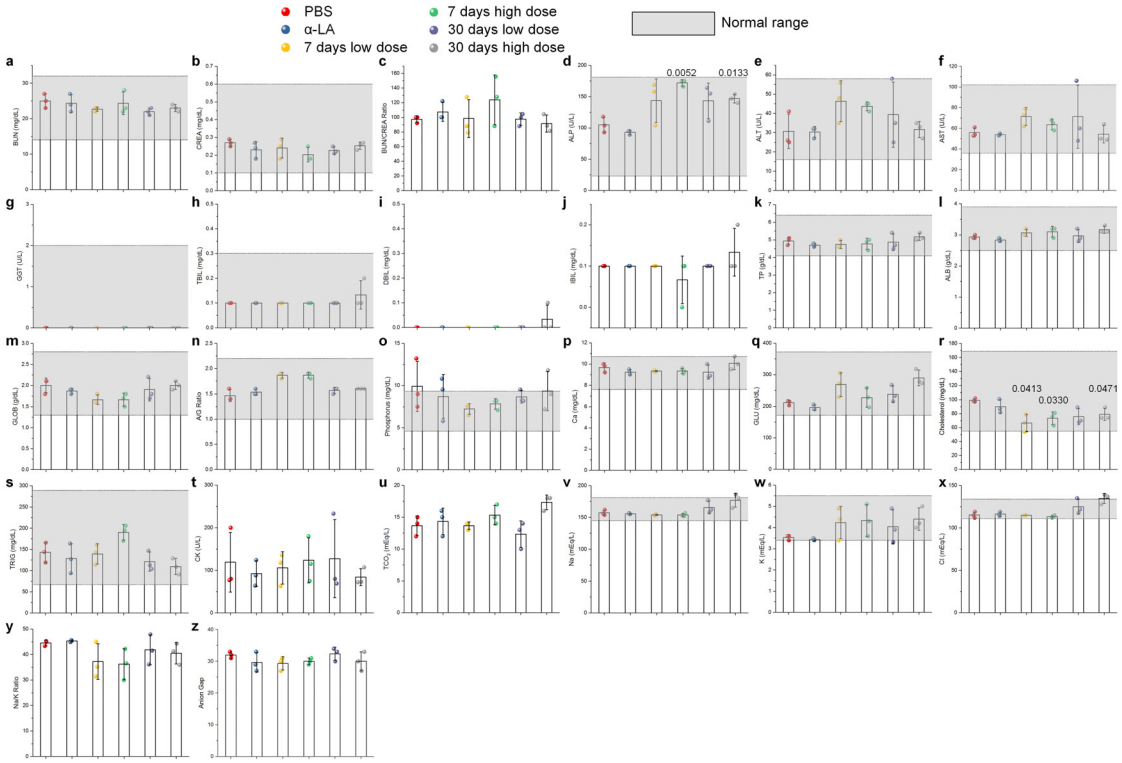

Supplementary Fig. 35 | Clinical chemistry analysis. Indicators are as below (n=3 biologically independent animals): **(a)** blood urea nitrogen (BUN), **(b)** creatinine (CREA), **(c)** BUN/CREA ratio, **(d)** alkaline phosphatase (ALP), **(e)** alanine aminotransferase (ALT), **(f)** aspartate aminotransferase (AST), **(g)** gamma-glutamyl transpeptidase (GGT), **(h)** total bilirubin (TBIL), **(i)** direct bilirubin (DBIL), **(j)** indirect bilirubin (IBIL), **(k)** total protein (TP), **(l)** albumin (ALB), **(m)** globulin (GLOB), **(n)** albumin to globulin (A/G) ratio, **(o)** phosphorus, **(p)** calcium, **(q)** glucose (GLU), **(r)** cholesterol, **(s)** triglycerides (TRIG), **(t)** creatine kinase (CK), **(u)** total carbon dioxide (TCO_2), **(v)** sodium, **(w)** potassium, **(x)** chloride, **(y)** Na/K ratio and **(z)** anion gap. Compared to PBS and α-LA controls, the high dose of AuQC$_{705}$ increased ALP after 7 and 30 days. Interestingly, serum cholesterol levels dropped on day 7 for both doses and on day 30 for the high dose, possibly due to the lipid binding property of α-LA[13]. To note, all indicators including ALP and cholesterol fall in their normal ranges.

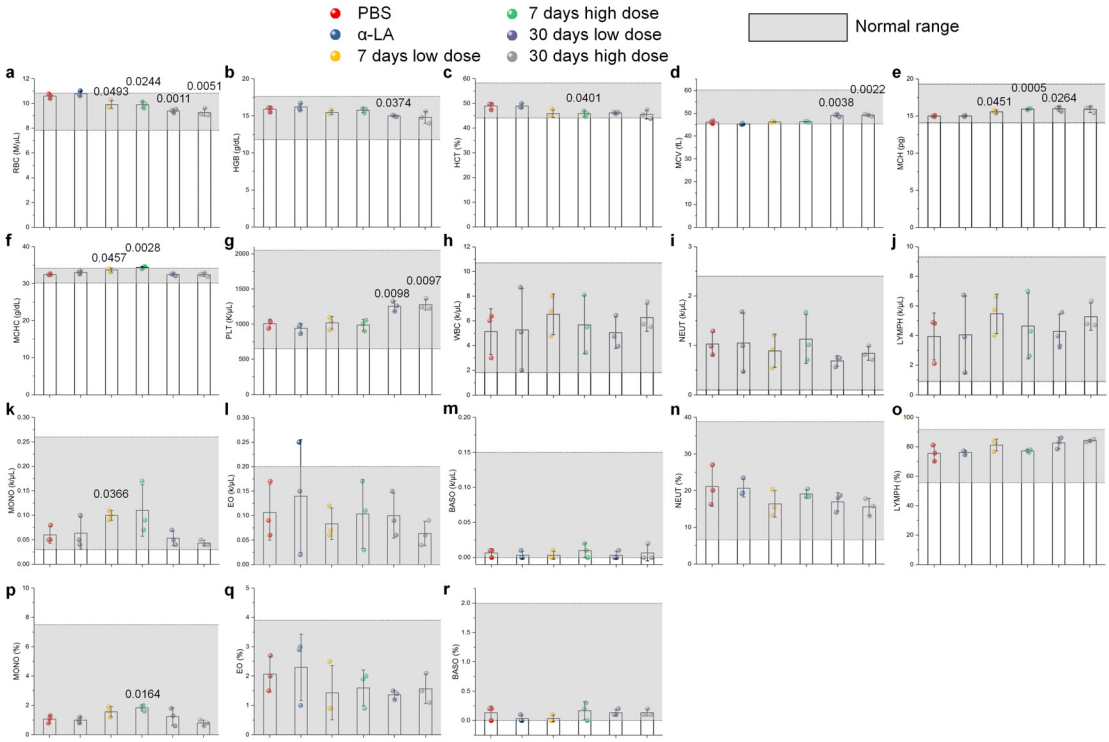

Supplementary Fig. 36 | Complete blood count with automated differentials. Indicators are as below (n=3 biologically independent animals): **(a)** red blood cell count (RBC), **(b)** hemoglobin (HGB), **(c)** hematocrit (HCT), **(d)** mean corpuscular volume (MCV), **(e)** mean corpuscular hemoglobin (MCH), **(f)** mean corpuscular hemoglobin concentration (MCHC), **(g)** platelet count (PLT), **(h)** white blood cell count (WBC), **(i)** neutrophil count (NEUT), **(j)** lymphocyte count (LYMPH), **(k)** monocyte count (MONO), **(l)** eosinophil count (EO), **(m)** basophil count (BASO), **(n)** neutrophil percentage, **(o)** lymphocyte percentage, **(p)** monocyte percentage, **(q)** eosinophil percentage and **(r)** basophil percentage. Compared to PBS and α-LA controls, RBC slightly dropped 7 and 30 days after injection of $AuQC_{705}$ at both doses; MCV and PLT increased on day 30 for both doses; MCH and MCHC increased after 7 days. Although some indicators as above are statistically significant, they are biologically non-significant and all indicators fall in the normal ranges.

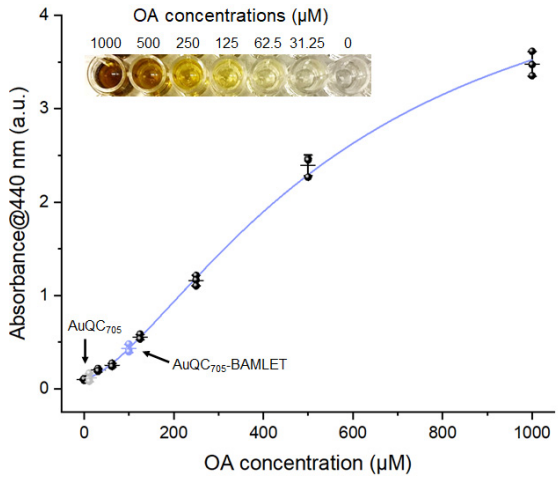

Supplementary Fig. 37 | Determination of oleic acid (OA) in the AuQC$_{705}$-BAMLET complex. Standards of OA at 31.25, 62.5, 125, 250, 500 and 1000 μM were fitted to a four-parameter logistic regression model (*R*=0.996). Measurements were first averaged and then fitted into the model to derive the OA content. The ratio of OA to α-LA in the AuQC$_{705}$-BAMLET complex is calculated to be 3.013±0.280, while in the AuQC$_{705}$ control which does not contain OA, the ratio is quantified to be 0.022±0.005.

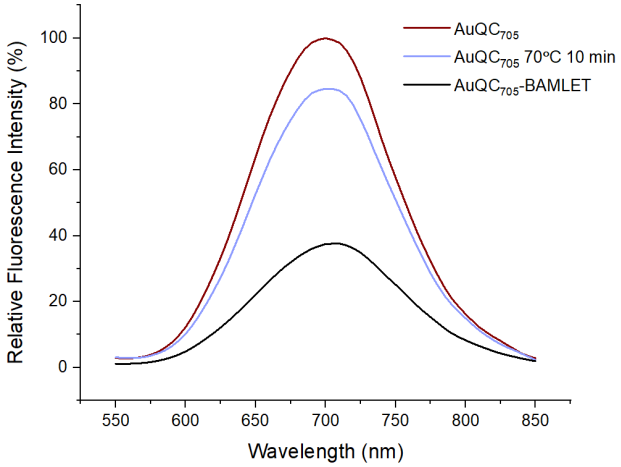

Supplementary Fig. 38 | Interaction between AuQC$_{705}$ and OA at alkaline conditions. Fluorescence emission spectra of AuQC$_{705}$, AuQC$_{705}$ after 10 min heat shock at 70°C in the absence and presence of 20% v/v OA at pH 11.5. Both high-temperature thermal treatment and BAMLET formation via OA binding led to quenching of NIR fluorescence. Such quenching is probably induced by hydrophobic interaction-mediated self-aggregation of α-LA which is facilitated at high pH, high temperature and in the presence of OA.

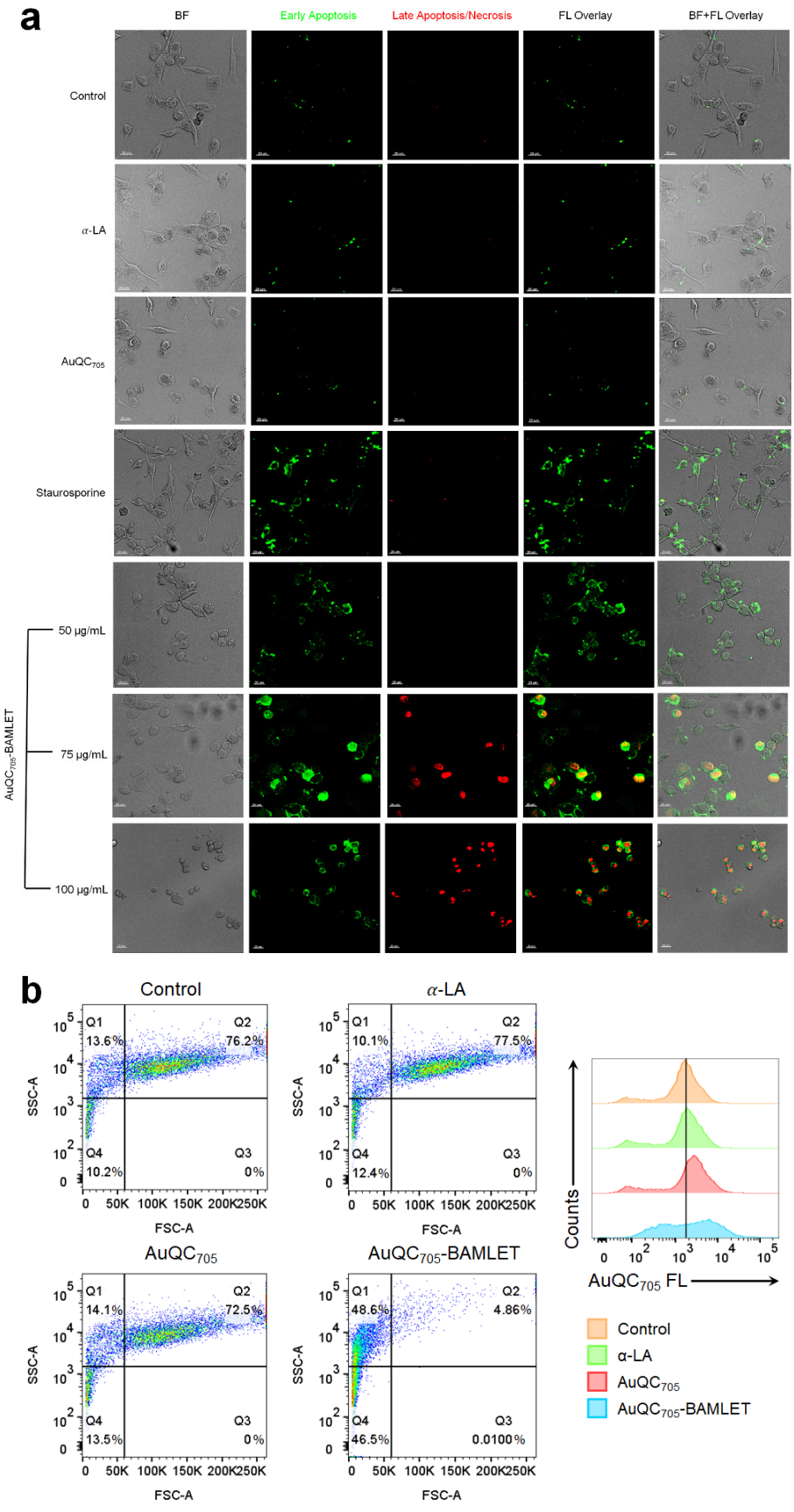
a
BF
Early Apoptosis
Late Apoptosis/Necrosis
FL Overlay
BF+FL Overlay
Control
α-LA
AuQC705
Staurosporine
AuQC705-BAMLET
50 μg/mL
75 μg/mL
100 μg/mL
b
Control
α-LA
AuQC705
AuQC705-BAMLET
SSC-A
FSC-A
Q1 13.6% Q2 76.2% Q4 10.2% Q3 0%
Q1 10.1% Q2 77.5% Q4 12.4% Q3 0%
Q1 14.1% Q2 72.5% Q4 13.5% Q3 0%
Q1 48.6% Q2 4.86% Q4 46.5% Q3 0.0100%
Counts
AuQC705 FL
Control
α-LA
AuQC705
AuQC705-BAMLET

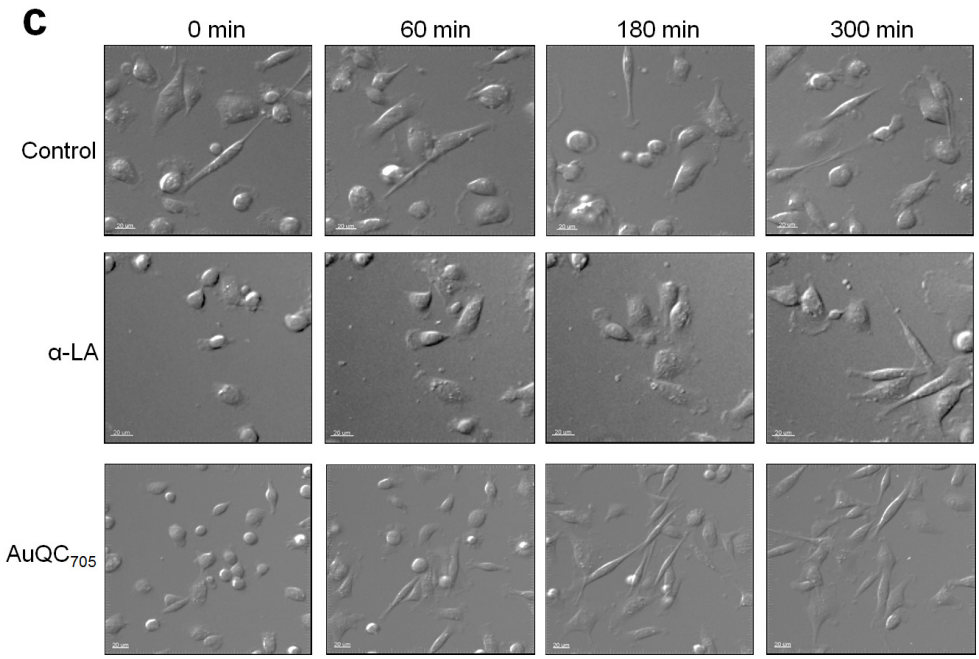

Supplementary Fig. 39 | Anti-cancer effects of AuQC$_{705}$-BAMLET. (a) Confocal fluorescence microscopic images of MDA-MB-231 cells co-stained with Annexin V and EthD-III for apoptosis and necrosis after treatment of α-LA, AuQC$_{705}$ and AuQC$_{705}$-BAMLET. Staurosporine was used as the positive control. AuQC$_{705}$-BAMLET at a low concentration (50 μg/mL) induced early apoptosis with surface translocation (green) of PS similar to staurosporine. As concentrations increased, higher populations of late apoptosis and necrosis (red) marked by membrane permeation were evident. Scale bars: 20 μm. **(b)** Scatter plots of MDA-MB-231 cells after 3 h treatment of control, α-LA, AuQC$_{705}$ and AuQC$_{705}$-BAMLET (100 μg/mL). In early apoptosis, only forward scatter (FSC) reflecting cell size decreases due to cell shrinkage and condensation, but both FSC and side scatter (SSC, indicating cell granularity) sharply decrease in advanced apoptosis and necrosis which ruptures plasma membranes and releases cellular contents[14]. An increase in AuQC$_{705}$ fluorescence from AuQC$_{705}$-BAMLET treatment can also be observed. Quadrant 1 (Q1): early apoptosis; Q2: live cells; Q4: late apoptosis and necrosis. **(c)** Time-lapse differential interference contrast microscopy of MDA-MB-231 cells treated by PBS, α-LA and AuQC$_{705}$ (refer to Supplementary Videos 2-4 for details). Scale bars: 20 μm.

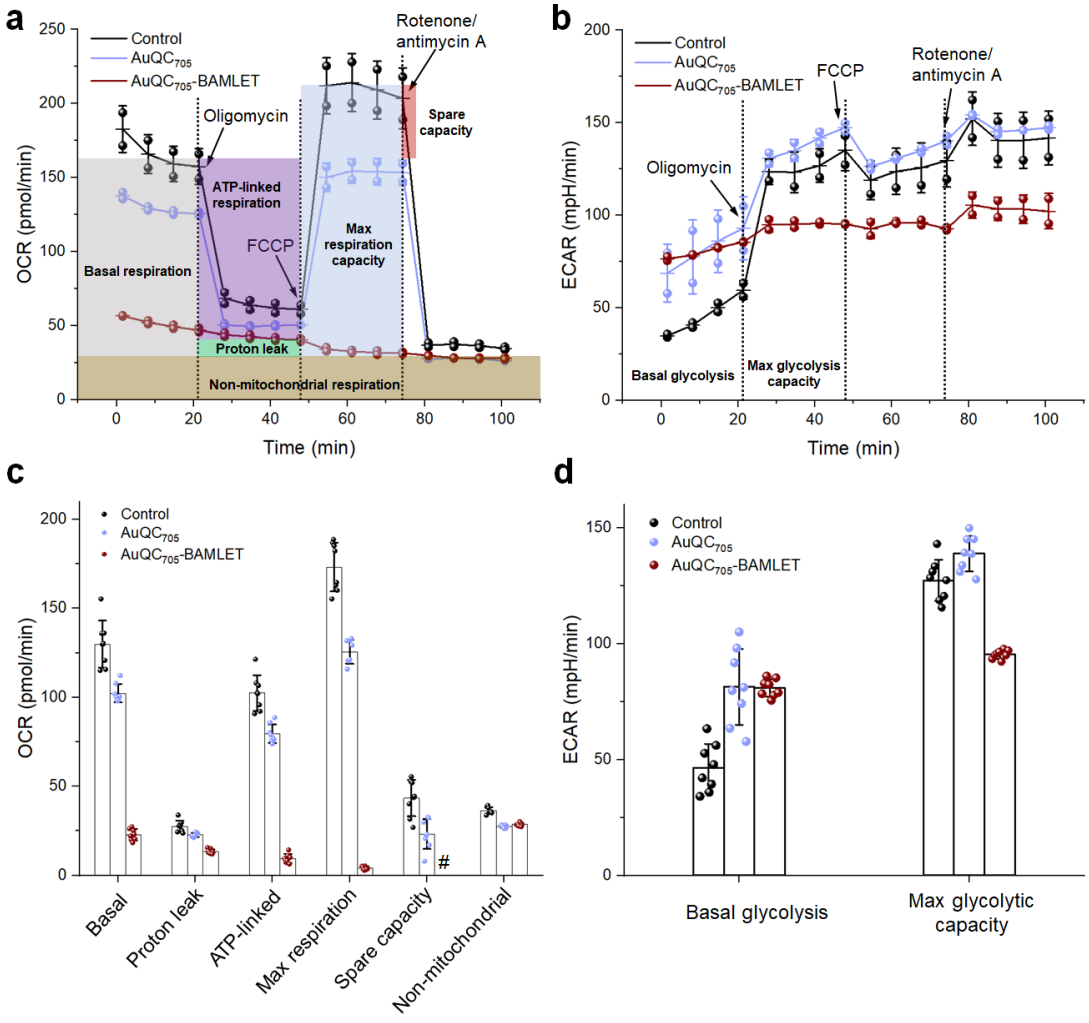

Supplementary Fig. 40 | Cell mitochondrial stress tests for MDA-MB-231 cells. Cells were treated with $AuQC_{705}$ or $AuQC_{705}$-BAMLET**.** Profiles of **(a)** the oxygen consumption rate (OCR) and **(b)** the extracellular acidification rate (ECAR) with arrows indicating injections of specific stressors: ATP synthase inhibitor oligomycin that reduces OCR and ATP production; oxidative phosphorylation uncoupler carbonyl cyanide *p*-trifluoromethoxy phenylhydrazone (FCCP) that disrupts mitochondrial membrane potential and proton gradients; rotenone/antimycin A that completely eliminates mitochondrial respiration. Duplicate measurements were carried out. Individual calculated parameters of **(c)** mitochondrial function and **(d)** glycolysis averaged during the corresponding processes. The # sign indicates no meaningful spare respiratory capacity can be obtained (negative values). Compared to the control cells, $AuQC_{705}$ slightly decreases basal, ATP-linked, maximal and non-mitochondrial respiration as well as spare respiratory capacity, whereas $AuQC_{705}$-BAMLET significantly decreases all respiration. In contrast, basal glycolytic machinery is boosted by both $AuQC_{705}$ and $AuQC_{705}$-BAMLET, but maximal glycolytic capacity is only decreased by $AuQC_{705}$-BAMLET.

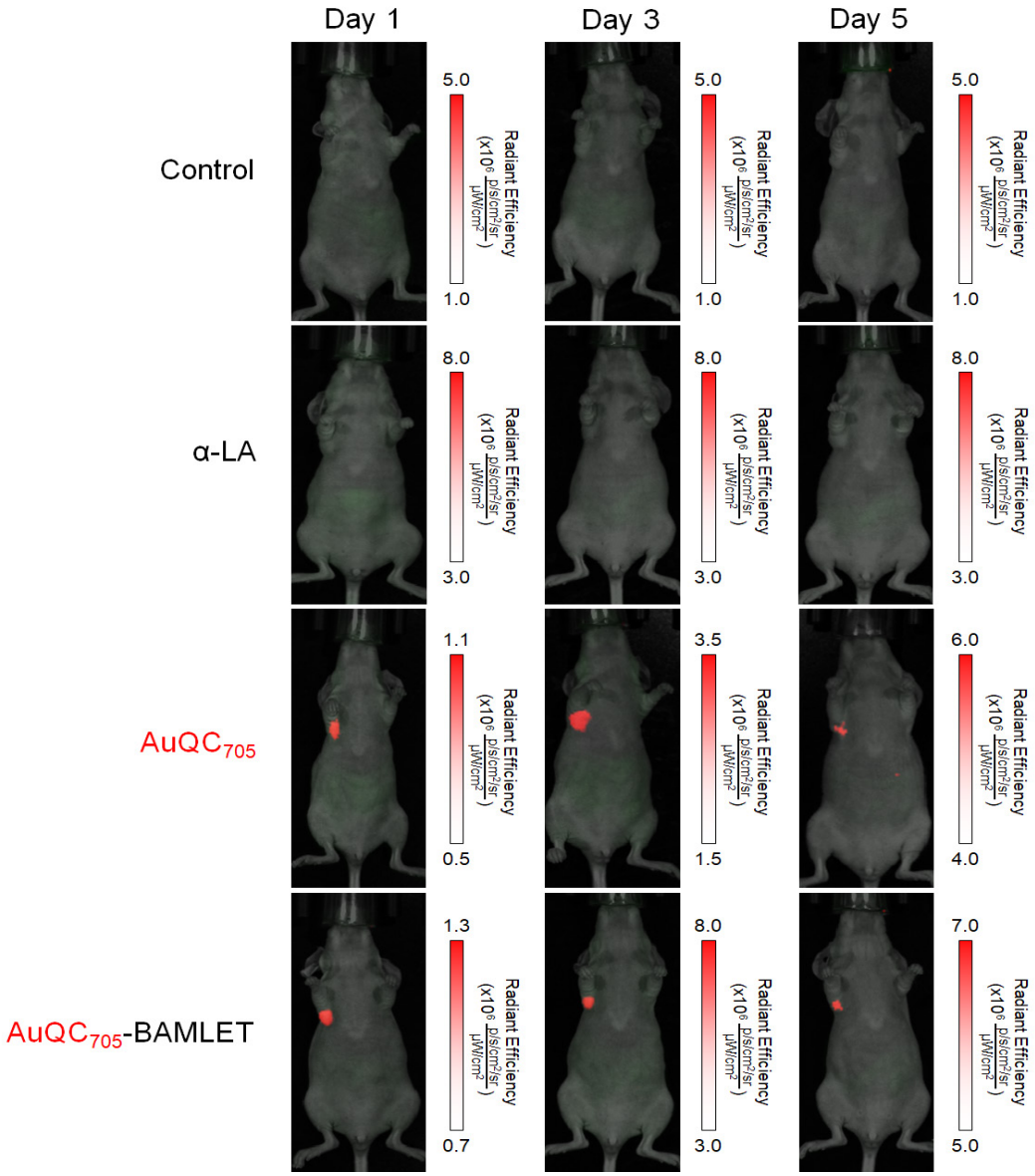

Supplementary Fig. 41 | Image-guided anti-cancer therapy in mice using AuQC$_{705}$-BAMLET. Fluorescence images of J:NU mice at different time points after co-implantation of MDA-MB-231 cancer cells with PBS, α-LA, AuQC$_{705}$ and AuQC$_{705}$-BAMLET (n=3 biologically independent animals). Despite the low injection doses, signals of both AuQC$_{705}$ and AuQC$_{705}$-BAMLET remained detectable for 5 days after grafting and were retained in the tumour region. Fluorescence signals could barely be differentiated from background after 5 days.

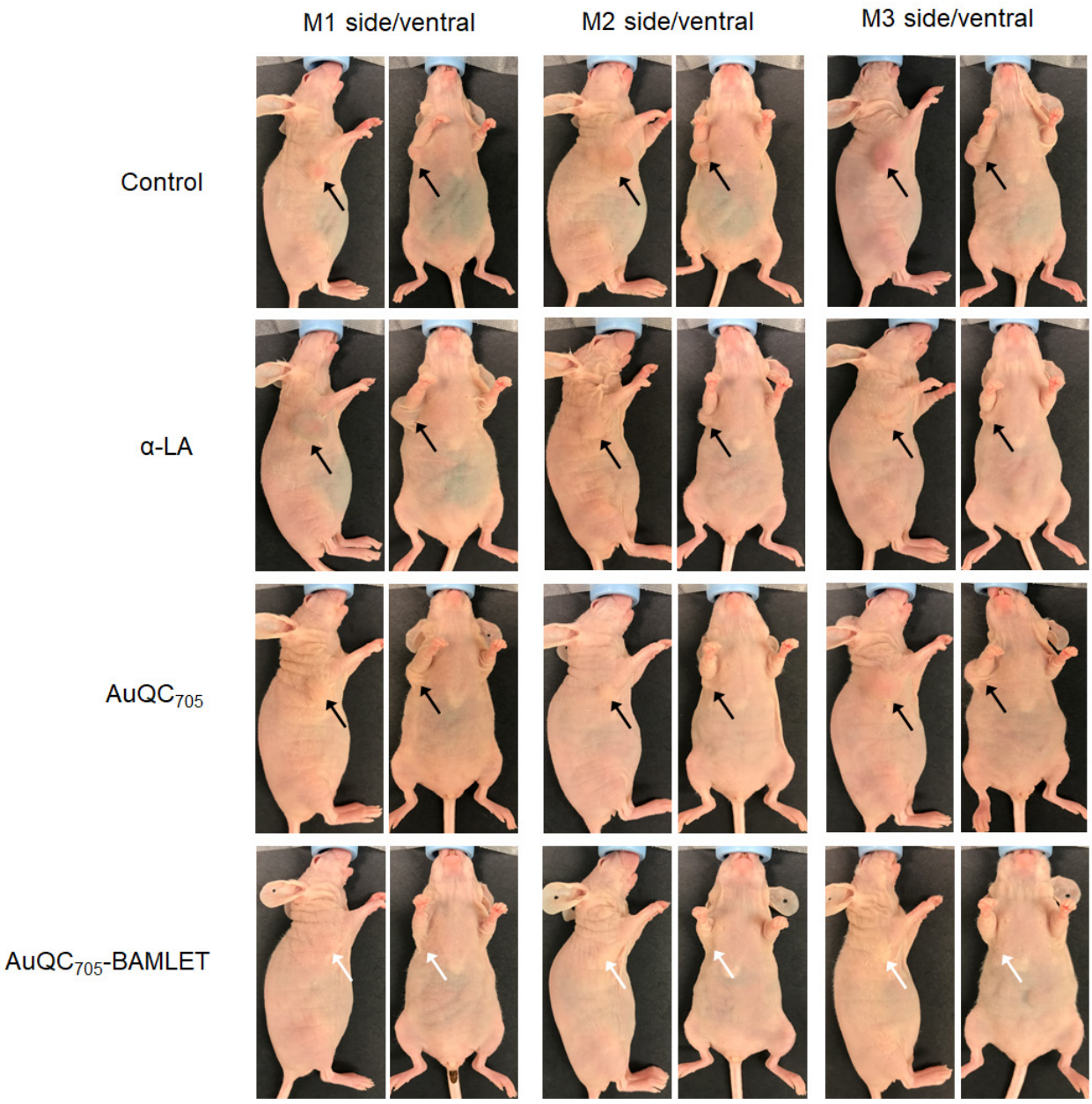

Supplementary Fig. 42 | Inhibition of breast tumour growth by $AuQC_{705}$-BAMLET. Photographs of NU/J mice at ventral and side positions for clearer views of tumour volumes 30 days after co-implantation of MDA-MB-231 cancer cells with PBS, α-LA, $AuQC_{705}$ or $AuQC_{705}$-BAMLET. Palpable tumours are indicated by black arrows and white arrows indicate where the tumours were originally grafted.

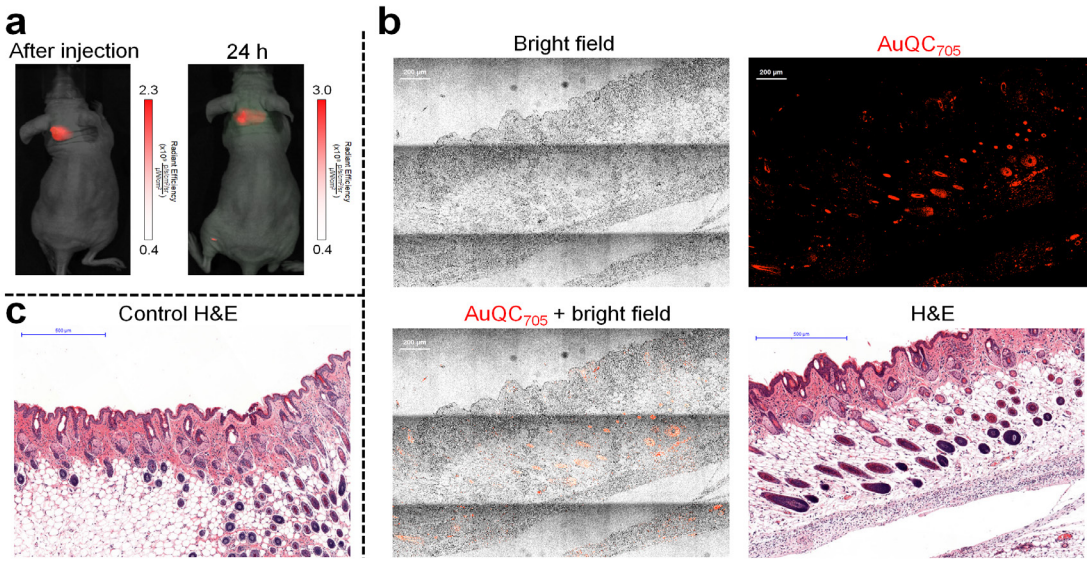

Supplementary Fig. 43 | AuQC$_{705}$-BAMLET has minor effects on healthy skin tissues. **(a)** Fluorescence imaging of J:NU mice after subcutaneous injection of AuQC$_{705}$-BAMLET. AuQC$_{705}$-specific fluorescence provided image-guidance to locate distribution of AuQC$_{705}$-BAMLET in skin. Most AuQC$_{705}$-BAMLET was retained near the injection site and only minor diffusion and release to the surrounding tissues was observed after 24 h. **(b)** Ex vivo fluorescence images of the skin from a J:NU mouse dissected under fluorescence image-guidance of AuQC$_{705}$-BAMLET. Uptake in the epidermis and papillary dermis was low. H&E staining was shown for histopathological evaluation. **(c)** H&E staining of a normal skin from a J:NU mouse.

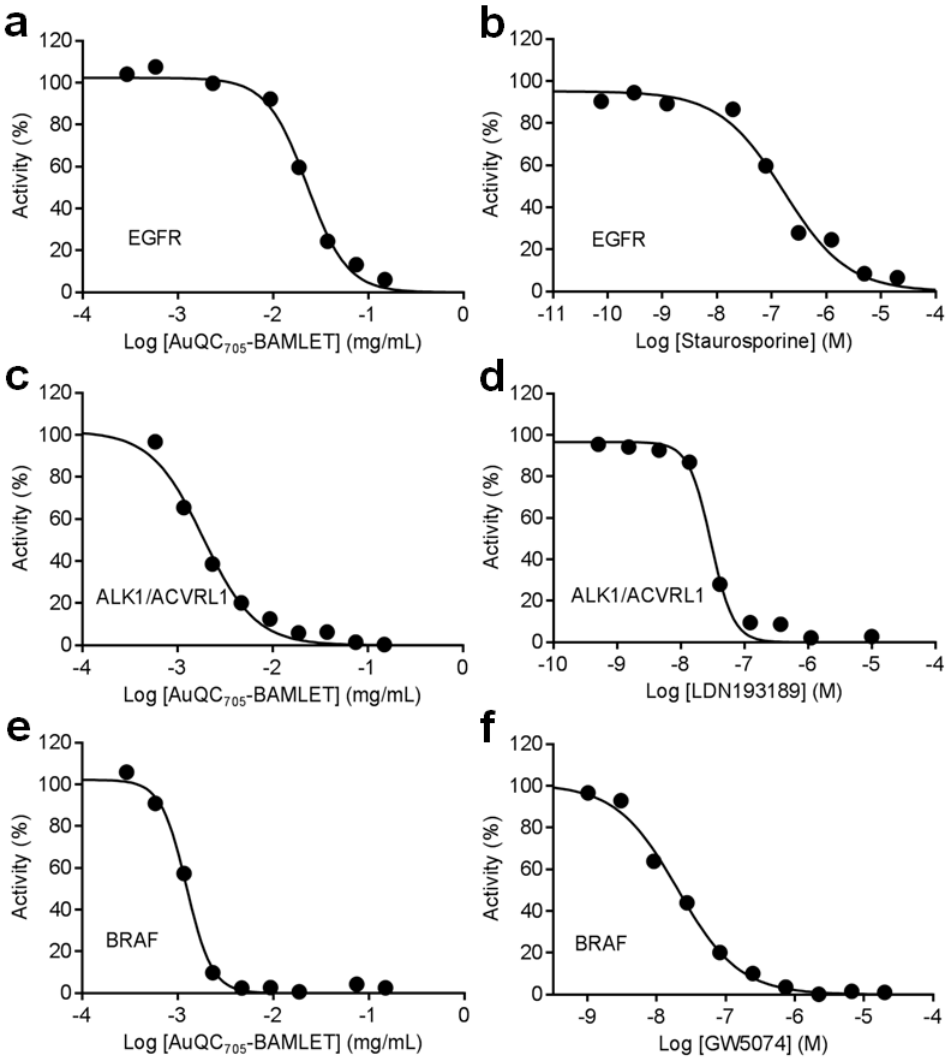

Supplementary Fig. 44 | Dose-response curves of $AuQC_{705}$-BAMLET defining IC_{50} values of kinases. **(a)** EGFR, **(c)** ALK1/ACVRL1 and **(e)** BRAF were shown with corresponding well-established inhibitors of **(b)** staurosporine, **(d)** LDN193189 and **(f)** GW5074 respectively, as positive controls. Data were fitted by sigmoidal dose-response curves. IC_{50} values of $AuQC_{705}$-BAMLET for EGFR, ALK1 and BRAF (22.83, 1.88 and 1.24 μg/mL Au) are calculated to be 1.1 μM, 89.2 nM and 58.8 nM (assuming an equivalent molarity of $Au_{32}/_{38}$ with no other constituents, resulting in an averaged $AuQC_{705}$ molecular mass=21,073 g/mol). IC_{50} values of specific control inhibitors staurosporine, LDN193189 and GW5074 are quantified to be 166.1, 29.9 and 20.2 nM for EGFR, ALK1 and BRAF.

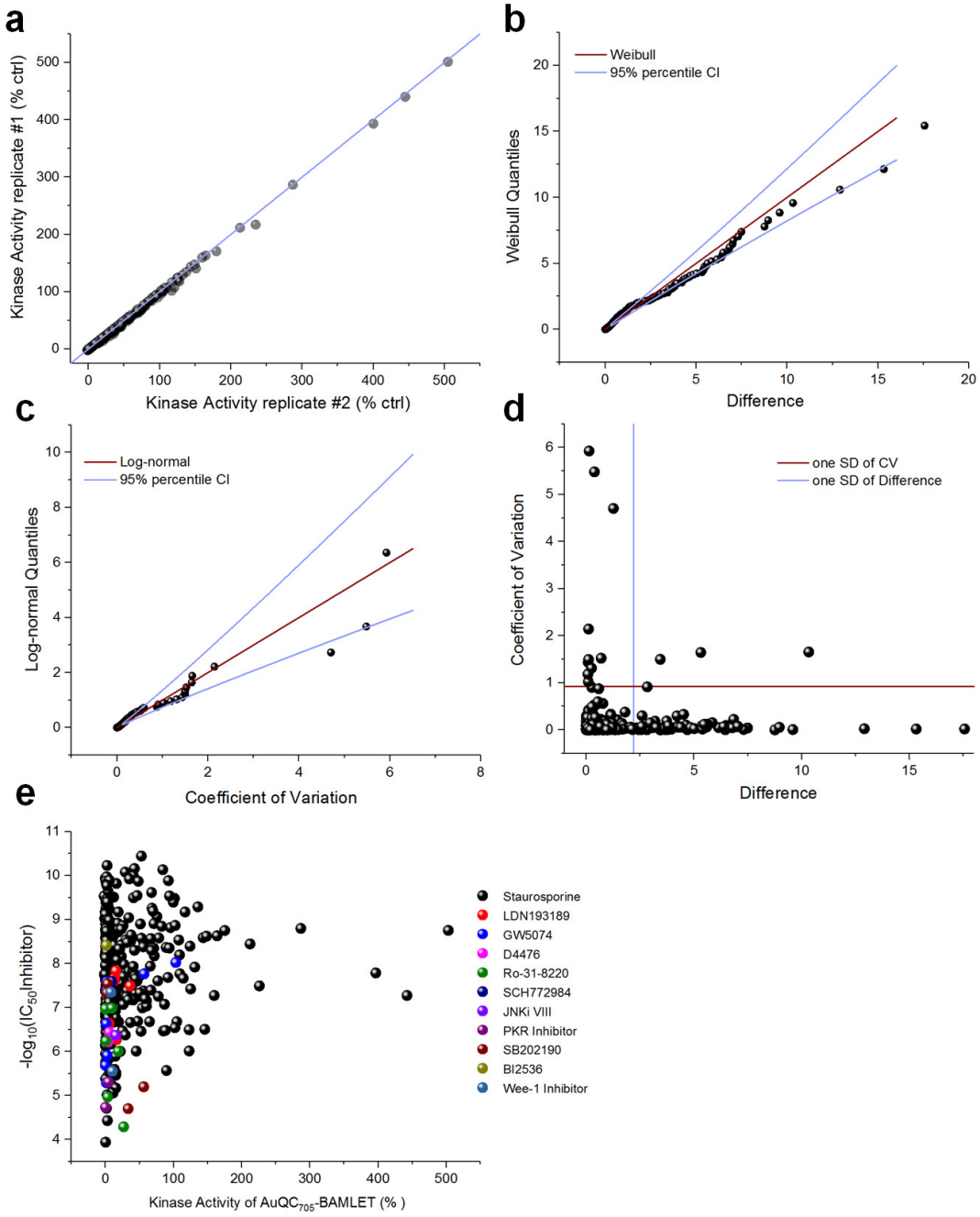

Supplementary Fig. 45 | Analysis on the interaction of AuQC$_{705}$-BAMLET with the wild-type human kinome. (a) Scatter plot of kinase activities of replicate 1 and 2 from inhibition of AuQC$_{705}$-BAMLET on all kinase targets. **(b)** Quantile-quantile plot of absolute difference from duplicate observations for kinase-AuQC$_{705}$-BAMLET pairs following Weibull distribution. 95% confidence intervals are outlined. **(c)** Quantile-quantile plot of coefficient of variation (CV) from duplicate observations for kinase-AuQC$_{705}$-BAMLET pairs following lognormal distribution. 95% confidence intervals are outlined. **(d)** Scatter plot of CV over absolute difference for all kinase targets influenced by AuQC$_{705}$-BAMLET. There are no outliers identified at thresholds of one standard deviation of CV (red line) and difference (blue line). **(e)** Absence of correlation between gold standard kinase inhibitors and AuQC$_{705}$-BAMLET against wild-type human kinome.

a

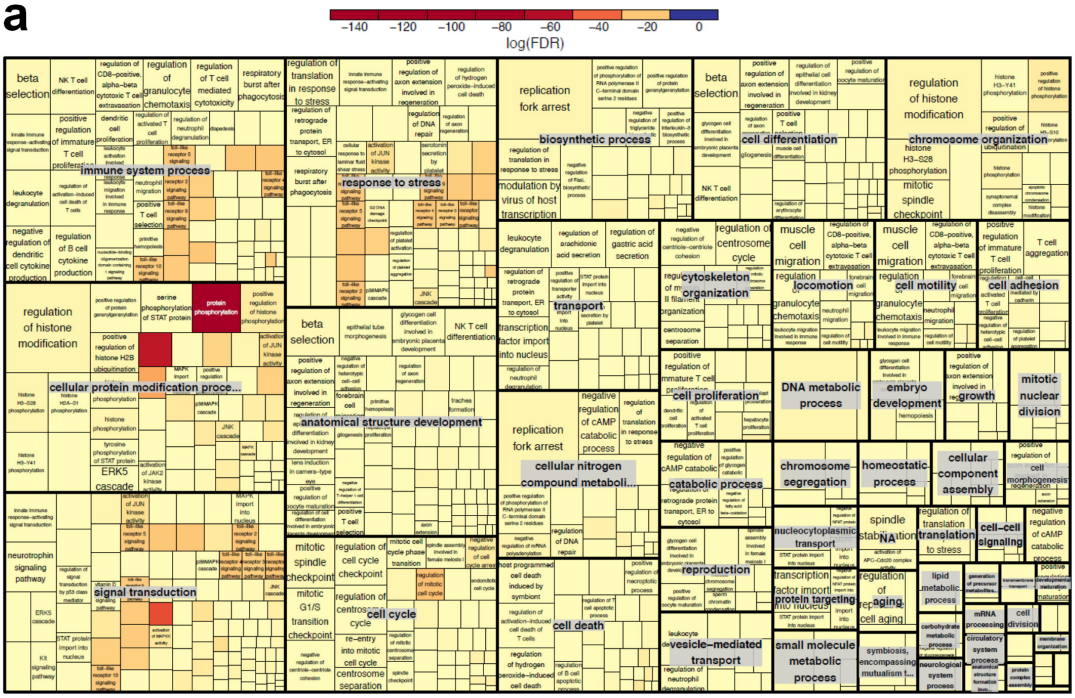
−140 −120 −100 −80 −60 −40 −20 0
log(FDR)
beta selection
NK T cell differentiation
regulation of CD8−positive, alpha−beta cytotoxic T cell extravasation
regulation of granulocyte chemotaxis
regulation of T cell mediated cytotoxicity
respiratory burst after phagocytosis
positive regulation of immature T cell proliferation
dendritic cell proliferation
regulation of activated T cell proliferation
regulation of neutrophil degranulation
innate immune response−activating signal transduction
immune system process
leukocyte degranulation
regulation of activation−induced cell death of T cells
neutrophil migration
positive T cell selection
negative regulation of dendritic cell cytokine production
regulation of B cell cytokine production
primitive hemopoiesis
regulation of translation in response to stress
regulation of retrograde protein transport, ER to cytosol
response to stress
regulation of axon extension involved in regeneration
regulation of DNA repair
positive regulation of axon extension involved in regeneration
regulation of hydrogen peroxide−induced cell death
cellular response to lamina fluid shear stress
activation of JUN kinase activity
respiratory burst after phagocytosis
JNK cascade
replication fork arrest
biosynthetic process
regulation of translation in response to stress
modulation by virus of host transcription
negative regulation of fast, biosynthetic process
beta selection
positive regulation of axon extension involved in regeneration
cell differentiation
glycogen cell differentiation involved in embryonic placenta development
NK T cell differentiation
regulation of anchorage
regulation of histone modification
histone H3−S28 phosphorylation
mitotic spindle checkpoint
chromosome organization
histone H3−T41 phosphorylation
positive regulation of histone phosphorylation
histone H3−K10 phosphorylation
leukocyte degranulation
leukocyte activation involved in inflammatory response
regulation of arachidonic acid secretion
regulation of gastric acid secretion
negative regulation of centriole−centriole cohesion
regulation of centrosome cycle
muscle cell migration
regulation of CD8−positive, alpha−beta cytotoxic T cell extravasation
muscle cell migration
positive regulation of immature T cell proliferation
T cell aggregation
regulation of histone modification
serine phosphorylation of STAT protein
protein phosphorylation
positive regulation of histone phosphorylation
positive regulation of protein geranylgeranylation
positive regulation of histone H2B ubiquitination
activation of JUN kinase activity
cellular protein modification proce...
histone H3−S28 phosphorylation
histone HDA−S1 phosphorylation
histone H3−T41 phosphorylation
histone phosphorylation
tyrosine phosphorylation of STAT protein
ERK5 cascade
activation of JAK2 kinase activity
beta selection
epithelial tube morphogenesis
glycogen cell differentiation involved in embryonic placenta development
NK T cell differentiation
positive regulation of axon extension involved in regeneration
regulation of axon regeneration
anatomical structure development
trachea formation
lens induction in camera−type eye
positive regulation of oocyte maturation
regulation of cell differentiation involved in embryonic placenta development
positive regulation of cell differentiation involved in kidney development
replication fork arrest
negative regulation of cAMP catabolic process
regulation of translation in response to stress
cellular nitrogen compound metaboli...
transport
regulation of retrograde protein transport, ER to cytosol
transcription factor import into nucleus
regulation of neutrophil degranulation
cytoskeleton organization
cell proliferation
negative regulation of cAMP catabolic process
catabolic process
regulation of retrograde protein transport, ER to cytosol
glycogen cell differentiation involved in embryonic placenta development
reproduction
DNA metabolic process
chromosome segregation
homeostatic process
cellular component assembly
positive regulation of cell component organization
locomotion
granulocyte chemotaxis
cell motility
cell adhesion
embryo development
growth
mitotic nuclear division
nucleocytoplasmic transport
RNA localization
transcription factor import into nucleus
protein targeting
spindle stabilization
regulation of translation
translation
cell−cell signaling
negative regulation of cell component organization
regulation of cell aging
cell aging
lipid metabolic process
mRNA processing
cell division
carbohydrate metabolic process
small molecule metabolic process
symbiosis, encompassing mutualism t...
circulatory system process
neurological system process
vesicle−mediated transport
regulation of neutrophil degranulation
innate immune response−activating signal transduction
neurotrophin signaling pathway
ERK5 cascade
signal transduction
mitotic spindle checkpoint
mitotic G1/S transition checkpoint
regulation of cell cycle checkpoint
regulation of centrosome cycle
re−entry into mitotic cell cycle
cell cycle
mitotic cell cycle phase transition
spindle assembly involved in female meiosis
negative regulation of cell cycle arrest
regulation of mitotic cell cycle
endoreduplication
cell cycle checkpoint
regulation of DNA repair
host programmed cell death induced by symbiont
regulation of activation−induced cell death of T cells
regulation of hydrogen peroxide−induced cell death
cell death
regulation of T cell apoptotic process
regulation of B cell apoptotic process

b

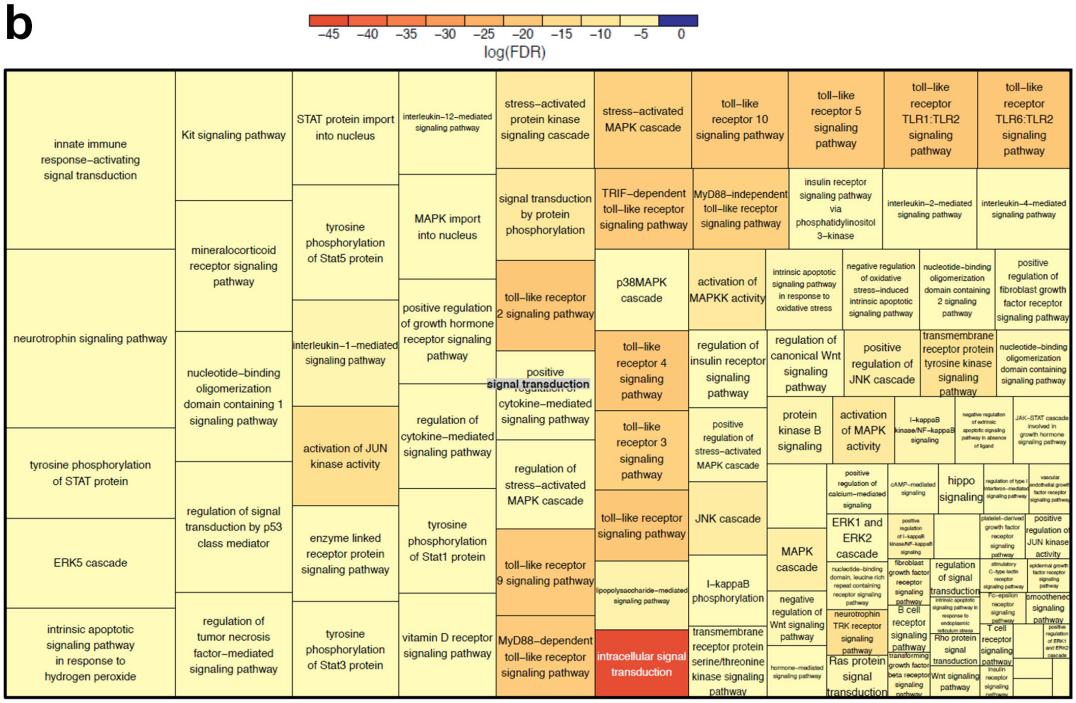
−45 −40 −35 −30 −25 −20 −15 −10 −5 0
log(FDR)
innate immune response−activating signal transduction
Kit signaling pathway
STAT protein import into nucleus
interleukin−12−mediated signaling pathway
stress−activated protein kinase signaling cascade
stress−activated MAPK cascade
toll−like receptor 10 signaling pathway
toll−like receptor 5 signaling pathway
toll−like receptor TLR1:TLR2 signaling pathway
toll−like receptor TLR6:TLR2 signaling pathway
tyrosine phosphorylation of Stat5 protein
MAPK import into nucleus
signal transduction by protein phosphorylation
TRIF−dependent toll−like receptor signaling pathway
MyD88−independent toll−like receptor signaling pathway
insulin receptor signaling pathway via phosphatidylinositol 3−kinase
interleukin−2−mediated signaling pathway
interleukin−4−mediated signaling pathway
mineralocorticoid receptor signaling pathway
neurotrophin signaling pathway
interleukin−1−mediated signaling pathway
positive regulation of growth hormone receptor signaling pathway
toll−like receptor 2 signaling pathway
p38MAPK cascade
activation of MAPKK activity
intrinsic apoptotic signaling pathway in response to oxidative stress
negative regulation of oxidative stress−induced intrinsic apoptotic signaling pathway
nucleotide−binding oligomerization domain containing 2 signaling pathway
positive regulation of fibroblast growth factor receptor signaling pathway
nucleotide−binding oligomerization domain containing 1 signaling pathway
positive signal transduction
cytokine−mediated signaling pathway
toll−like receptor 4 signaling pathway
regulation of insulin receptor signaling pathway
regulation of canonical Wnt signaling pathway
positive regulation of JNK cascade
transmembrane receptor protein tyrosine kinase signaling pathway
nucleotide−binding oligomerization domain containing signaling pathway
tyrosine phosphorylation of STAT protein
activation of JUN kinase activity
regulation of cytokine−mediated signaling pathway
regulation of stress−activated MAPK cascade
toll−like receptor 3 signaling pathway
positive regulation of stress−activated MAPK cascade
protein kinase B signaling
activation of MAPK activity
I−kappaB kinase/NF−kappaB signaling
negative regulation of extrinsic apoptotic signaling pathway in absence of ligand
JAK−STAT cascade involved in growth hormone signaling pathway
ERK5 cascade
enzyme linked receptor protein signaling pathway
tyrosine phosphorylation of Stat1 protein
toll−like receptor 9 signaling pathway
toll−like receptor signaling pathway
JNK cascade
positive regulation of calcium−mediated signaling
cAMP−mediated signaling
hippo signaling
regulation of type I interferon−mediated signaling pathway
vascular endothelial growth factor receptor signaling pathway
regulation of signal transduction by p53 class mediator
regulation of tumor necrosis factor−mediated signaling pathway
tyrosine phosphorylation of Stat3 protein
vitamin D receptor signaling pathway
MyD88−dependent toll−like receptor signaling pathway
lipopolysaccharide−mediated signaling pathway
intracellular signal transduction
I−kappaB phosphorylation
transmembrane receptor protein serine/threonine kinase signaling pathway
MAPK cascade
negative regulation of Wnt signaling pathway
hormone−mediated signaling pathway
ERK1 and ERK2 cascade
nucleotide−binding domain, leucine rich repeat containing receptor signaling pathway
neurotrophin TRK receptor signaling pathway
Ras protein signal transduction
positive regulation of I−kappaB kinase/NF−kappaB signaling
fibroblast growth factor receptor signaling pathway
transforming growth factor beta receptor signaling pathway
regulation of signal transduction
B cell receptor signaling pathway
Rho protein signal transduction
Wnt signaling pathway
platelet−derived growth factor receptor signaling pathway
stimulatory C−type lectin receptor signaling pathway
Fc−epsilon receptor signaling pathway
T cell receptor signaling pathway
insulin receptor signaling pathway
positive regulation of JUN kinase activity
epidermal growth factor receptor signaling pathway
smoothened signaling pathway
positive regulation of ERK1 and ERK2 cascade
intrinsic apoptotic signaling pathway in response to hydrogen peroxide

c

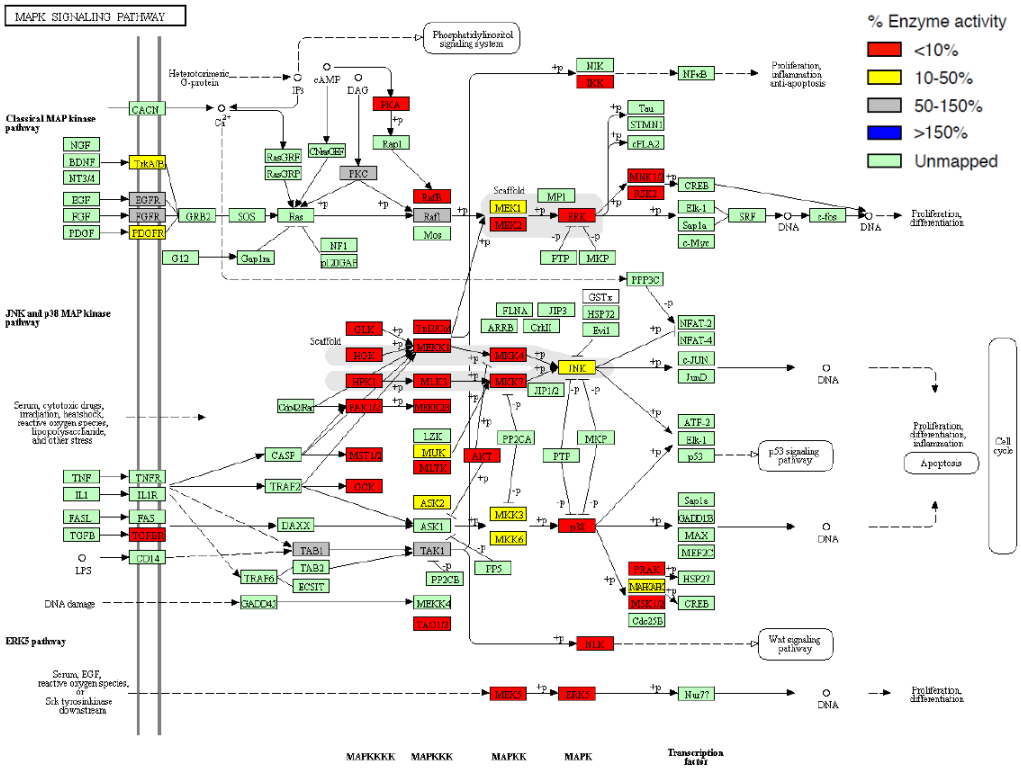
MAPK SIGNALING PATHWAY
% Enzyme activity
<10%
10-50%
50-150%
>150%
Unmapped
Classical MAP kinase pathway
JNK and p38 MAP kinase pathway
ERK5 pathway
MAPKKKK
MAPKKK
MAPKK
MAPK
Transcription factor

d

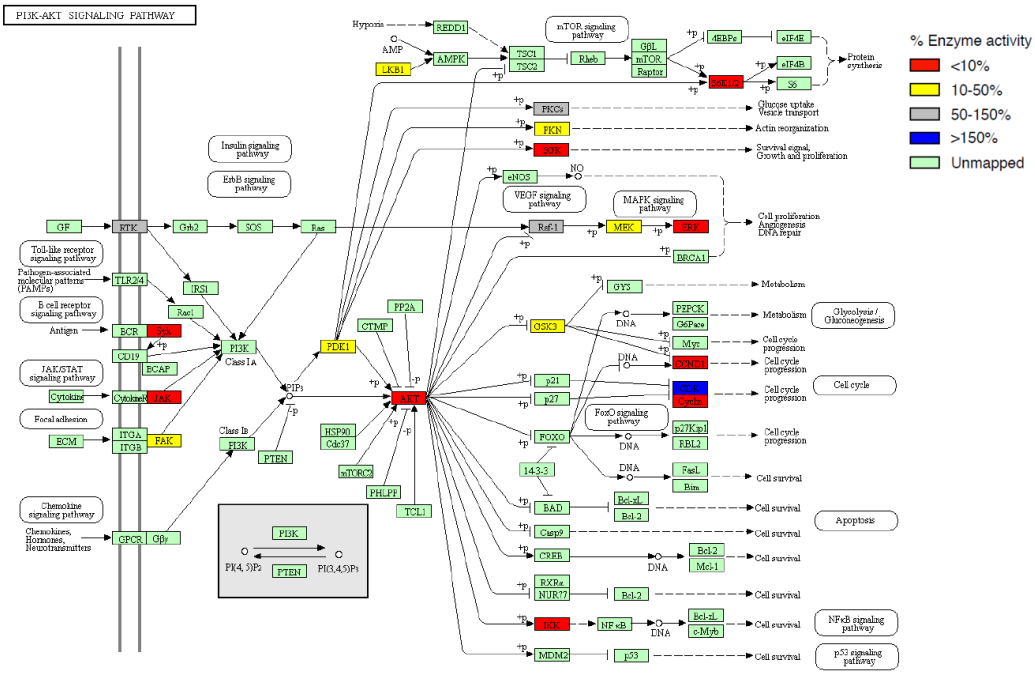
PI3K-AKT SIGNALING PATHWAY
% Enzyme activity
<10%
10-50%
50-150%
>150%
Unmapped

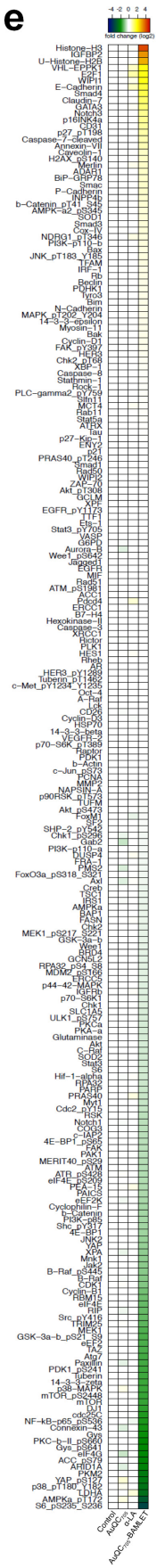
e
-4 -2 0 2 4
fold change (log2)
Histone−H3
IGFBP2
U−Histone−H2B
VHL−EPAS1
FoxP1
WIPI1
E−Cadherin
Smad4
Claudin−7
GATA3
Notch3
p16INK4a
GR31
p27_pT198
Caspase−7−cleaved
Annexin−VII
Caveolin−1
H2AX_pS140
Merlin
ADAR1
BiP−GRP78
Smac
P−Cadherin
INPP4B
b−Catenin_pT41_S45
AMPK−a2_pS345
SOD1
Smad3
Cox−IV
NDRG1_pT346
PI3K−p110−b
Bax
JNK_pT183_Y185
TFAM
IRF−1
Rb
Beclin
PDHK1
Tyro3
Bim
N−Cadherin
MAPK_pT202_Y204
14−3−3−epsilon
Myosin−11
Bak
Cyclin−D1
FAK_pY397
HER3
Chk2_p168
XBP−1
Caspase−8
Stathmin−1
Rock−1
PLC−gamma2_pY759
Sfn11
MCT4
Rab11
Stat5a
ATRX
Tau
p27−Kip1
ENO1
EGFR
PRAS40_pT246
Smad1
Integ5
WIP1
ZAP−70
Akt_pT308
GCLM
XPF
EGFR_pY1173
ITF1
Ets−1
Stat3_pY705
VASP
G6PD
Aurora−B
Wee1_pS642
Jagged1
EGFR
MIF
Rad51
ATM_pS1981
ASC
Cyclin−E1
ERCC1
B7−H4
Hexokinase−II
Caspase−3
XRCC1
Rictor
PTK1
HES1
Rheb
AR
HER3_pY1289
Tuberin_pT1462
c−Met_pY1234_Y1235
Oct−4
A−Raf
Ck
CD26
Cyclin−C3
HSP70
14−3−3−beta
VEGFR2
p70−S6K_pT389
Bid
Rictor
PDK1
b−Actin
c−Jun_pS73
PCNA
MMP−2
NAPSIN−A
p90RSK_pT573
TUFM
Akt_pS473
FoxM1
SF2
SHP−2_pY542
Chk1_pS296
Gab2
PI3K−p110−a
DUSP4
FRA−1
PMS2
FoxO3a_pS318_S321
Axl
Creb
TSC1
IRS1
AMPKa
PAI−1
FASN
CDK2
MEK1_pS217_S221
GSK−3a−b
Wee1
BRD4
GCN5L2
RPA32_pS4_S8
MDM2_pS166
ERCC3
p44−42−MAPK
IGFRb
p70−S6K1
Chk1
SLC1A5
ULK1_pS757
PKCa
PKA−a
Glutaminase
Akt
C−Raf
Sc735
Stat3
Jak1
Hif−1−alpha
RPA32
PAI1P
PRAS40
Myt1
Cdc2_pY15
Rsk
Notch1
CD33
c−IAP2
4E−BP1_pS65
FAK
PAK1
MERIT40_pS29
ATM
ATR_pS428
eIF4E_pS209
PEA−15
PAICS
eEF2k
Cyclophilin−F
b−Catenin
PI3K−p85
Shc_pY317
4E−BP1
JNK2
YAP
XPA
Mnk1
Jak2
B−Raf_pS445
B−Raf
CDK1
Cyclin−B1
RBM15
eIF4E
RIP
Src_pY416
TRIM25
MEK1
GSK−3a−b_pS21_S9
eEF2
TAZ
Alg7
Paxillin
PDK1_pS241
Tuberin
14−3−3−zeta
p38−MAPK
mTOR_pS2448
mTOR
Rb1
cdc25c
NF−kB−p65_pS536
Connexin−43
Gys
PKC−b−II_pS660
Gys_pS641
eIF4G1
ACC_pS79
ARID1A
PKM2
YAP_pS127
p38_pT180_Y182
LDHA
AMPKa_pT172
S6_pS235_S236
Control
AsPC−1
CLA
AsPC−1−BAMLET

f

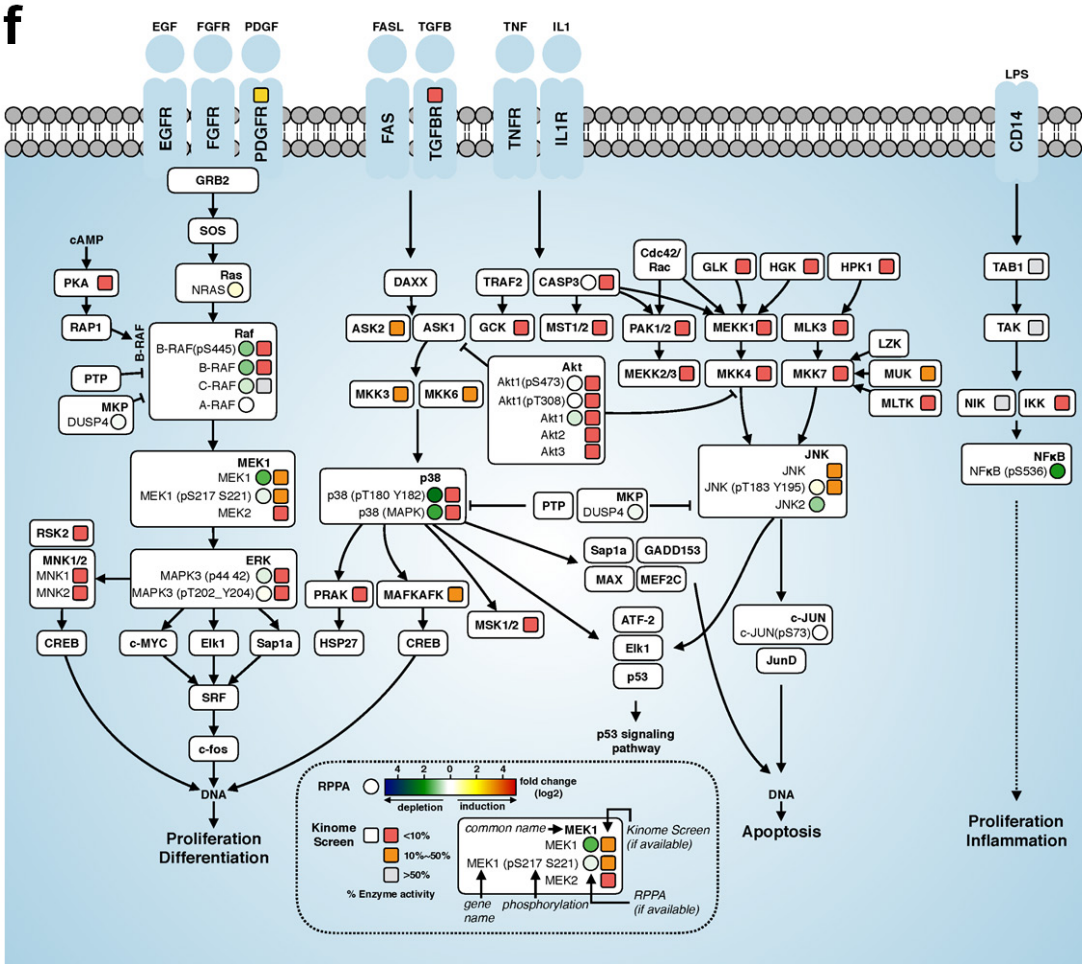
EGF
FGFR
PDGF
FASL
TGFB
TNF
IL1
LPS
EGFR
FGFR
PDGFR
FAS
TGFBR
TNFR
IL1R
CD14
GRB2
SOS
Ras
NRAS
cAMP
PKA
RAP1
B-RAF
PTP
MKP
DUSP4
Raf
B-RAF(pS445)
B-RAF
C-RAF
A-RAF
MEK1
MEK1
MEK1 (pS217 S221)
MEK2
RSK2
MNK1/2
MNK1
MNK2
ERK
MAPK3 (p44 42)
MAPK3 (pT202_Y204)
CREB
c-MYC
Elk1
Sap1a
SRF
c-fos
DNA
Proliferation
Differentiation
DAXX
TRAF2
CASP3
Cdc42/
Rac
GLK
HGK
HPK1
ASK2
ASK1
GCK
MST1/2
PAK1/2
MEKK1
MLK3
LZK
Akt
Akt1(pS473)
Akt1(pT308)
Akt1
Akt2
Akt3
MEKK2/3
MEKK4
MKK7
MUK
MLTK
MKK3
MKK6
p38
p38 (pT180 Y182)
p38 (MAPK)
PTP
MKP
DUSP4
JNK
JNK
JNK (pT183 Y195)
JNK2
Sap1a
GADD153
MAX
MEF2C
PRAK
MAFKAFK
MSK1/2
HSP27
CREB
ATF-2
Elk1
p53
p53 signaling
pathway
c-JUN
c-JUN(pS73)
JunD
DNA
Apoptosis
TAB1
TAK
NIK
IKK
NFκB
NFκB (pS536)
Proliferation
Inflammation
RPPA
4 2 0 2 4
fold change
(log2)
depletion
induction
Kinome
Screen
<10%
10%~50%
>50%
% Enzyme activity
common name
MEK1
MEK1
MEK1 (pS217 S221)
MEK2
Kinome Screen
(if available)
RPPA
(if available)
gene
name
phosphorylation

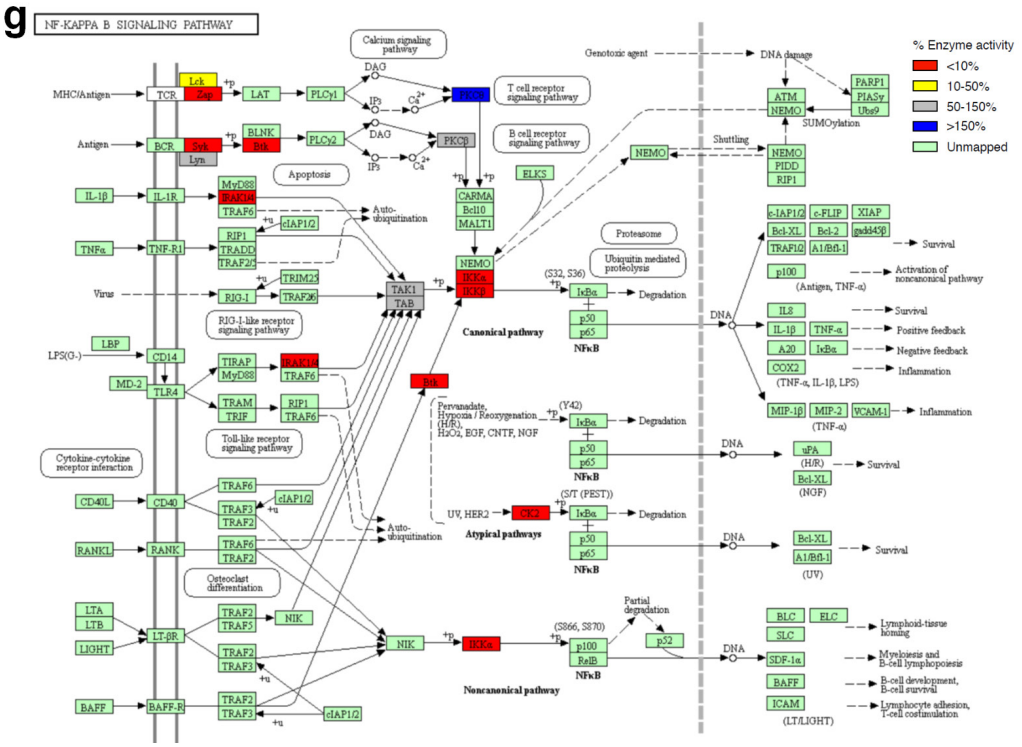

Supplementary Fig. 46 | Signaling pathway analysis of AuQC$_{705}$-BAMLET. (a) Full gene ontology (GO) treemap with input kinases of ⩾95% inhibition by AuQC$_{705}$-BAMLET. Box sizes and colours correspond to odds ratio and log(false discovery rate) (FDR) of GO-term enrichment for biological processes, respectively. Small boxes grouped together correlate with an upper hierarchy GO term in the middle of the large box. Fisher's exact test was used and data are referenced to UniProt human proteome database (number of proteins reviewed=20,203). **(b)** Treemap of GO enrichment analysis for signal transduction of AuQC$_{705}$-BAMLET. **(c)** KEGG (Kyoto Encyclopedia of Genes and Genomes) pathway analysis on MAPK signaling of AuQC$_{705}$-BAMLET. **(d)** KEGG pathway analysis of PI3K-AKT signaling of AuQC$_{705}$-BAMLET. **(e)** Heat map of key quality-control-passed biomarkers in the proteome of MDA-MB-231 breast cancer cells that were significantly altered by AuQC$_{705}$-BAMLET from quantitative RPPA. Colour bar shows $\log_2$-transformed fold change of protein expression normalized by control. **(f)** Signaling pathway of effector proteins influenced by AuQC$_{705}$-BAMLET. Regulations of kinase activities and expression were mapped from human kinome profiling and reverse-phase protein microarray (RPPA). **(g)** KEGG pathway analysis of NF-κB signaling of AuQC$_{705}$-BAMLET. Data were mapped based on kinase inhibitions with reference to KEGG pathway database. Nodes were labeled by gene names and colour-coded differently by inhibition levels. Red: strong inhibition; yellow: moderate inhibition; grey: low or no inhibition; blue: enhancement; green: unmapped).

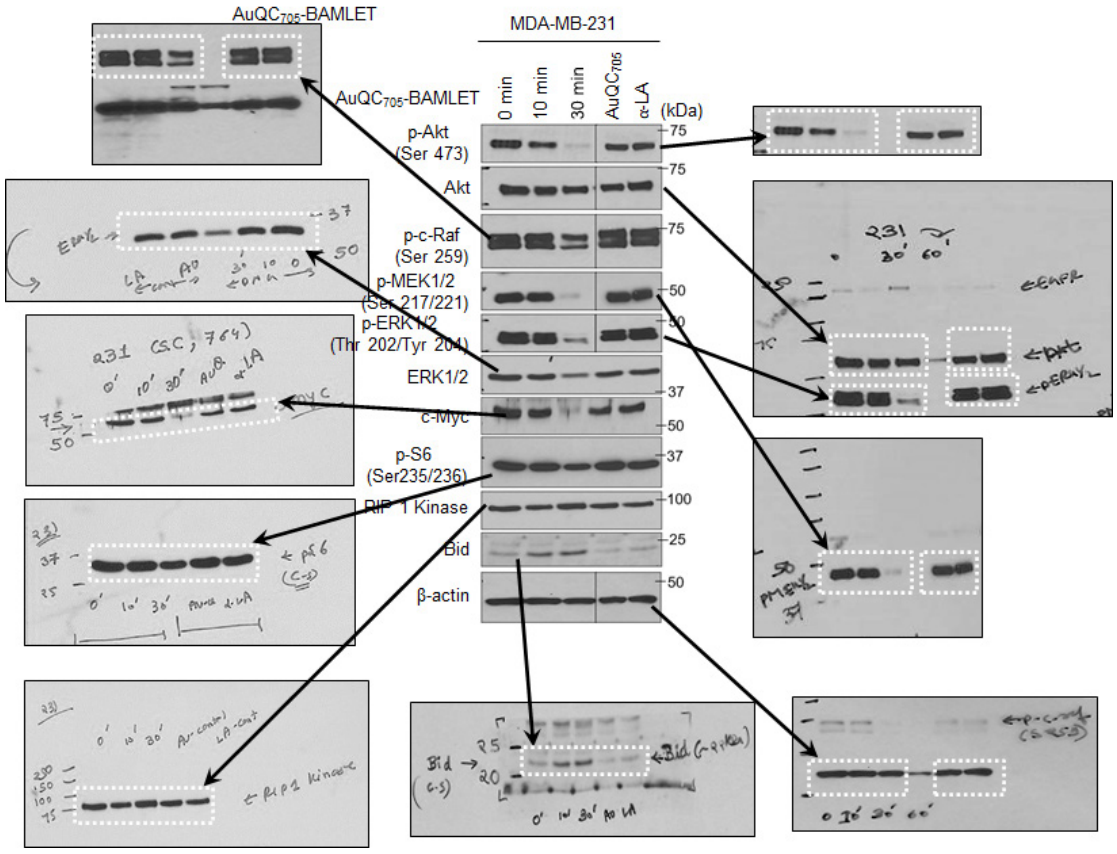

Supplementary Fig. 47 | Source blot data of Fig. 7d. Note that the blot image of total ERK1/2 should be flipped. In the meantime, we have observed decrease in the β-actin at 60 min, suggesting protein degradation as a consequence of cell death. Therefore, it does not help us pinpoint the implicated molecular mechanisms and was removed later on. Cropped bands were indicated as the dotted white boxes on the original gels.

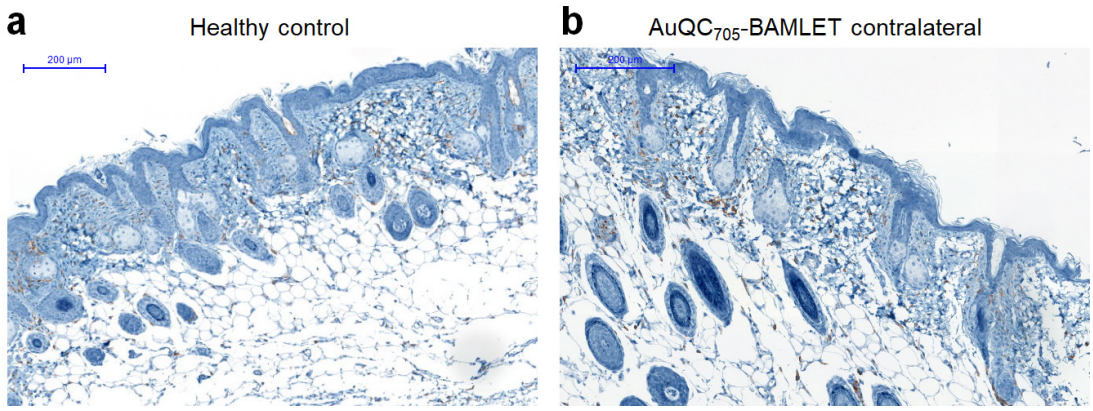

Supplementary Fig. 48 | Immunohistochemical (IHC) staining of Iba1 on skin tissues. Skin was resected from **(a)** a healthy J:NU mouse without injections and **(b)** the contralateral side of a J:NU mouse 24 h after subcutaneous injection of AuQC$_{705}$-BAMLET.

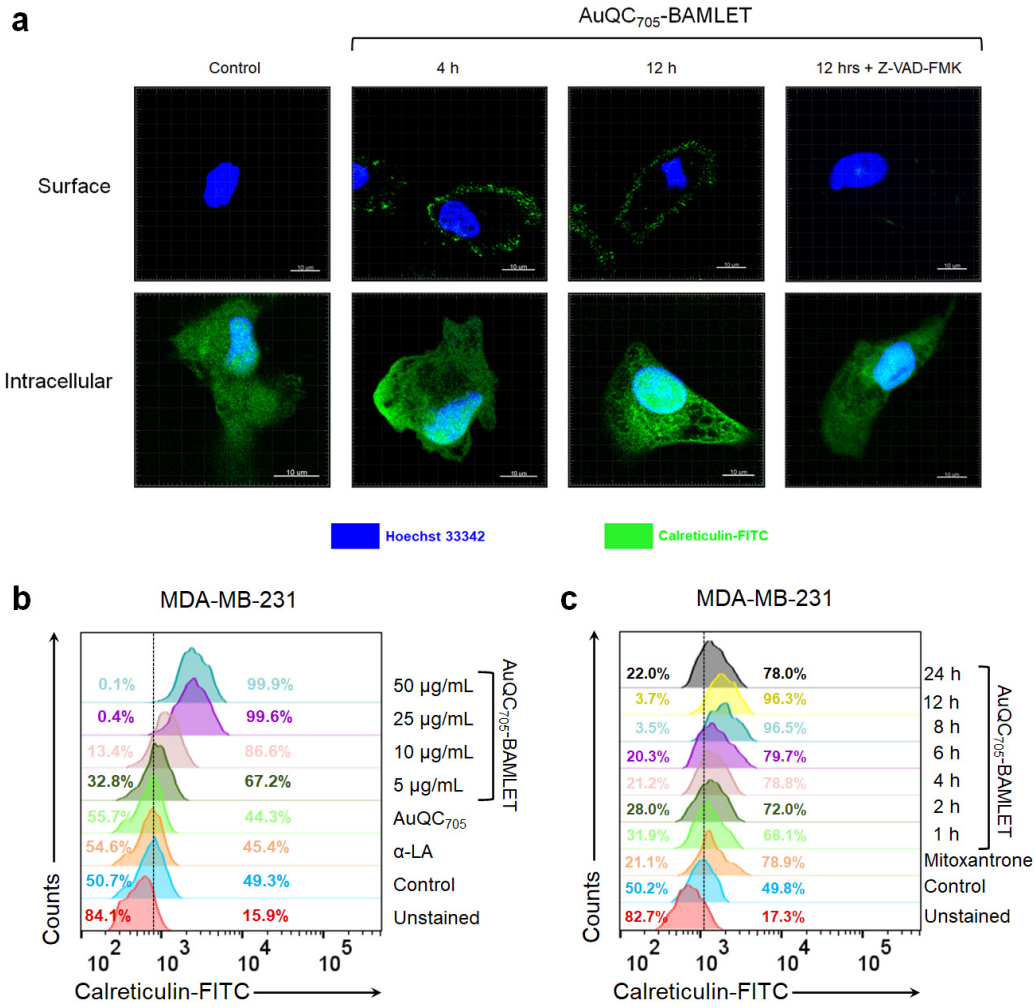

Supplementary Fig. 49 | AuQC$_{705}$-BAMLET induces potent immunogenic cancer cell death through surface translocation of calreticulin (CRT). (a) Immunofluorescence visualization of surface CRT in non-permeabilized live cells and intracellular CRT in permeabilized cells by confocal microscopy (green), after treatment of AuQC$_{705}$-BAMLET for 4 and 12 h. The elicited immunogenicity by AuQC$_{705}$-BAMLET dictated by surface CRT translocation can be inhibited by pan caspase inhibitor Z-VAD-FMK. **(b)** Detection of surface exposed CRT in MDA-MB-231 cells by immunofluorescence staining using flow cytometry. Both α-LA and AuQC$_{705}$ have a surface CRT level close to the control, while treatment with all concentrations of AuQC$_{705}$-BAMLET for 1 h can distinctly induce elevated surface translocation of CRT. **(c)** Kinetics of surface CRT translocation. MDA-MB-231 cells were treated with 5 μg/mL AuQC$_{705}$-BAMLET for the indicated time and 1 μM mitoxantrone treatment for 24 h was included as the positive control[15]. The induction of surface CRT by AuQC$_{705}$-BAMLET was detectable as early as 1 h after treatment and reached the maximum 8 h after treatment.

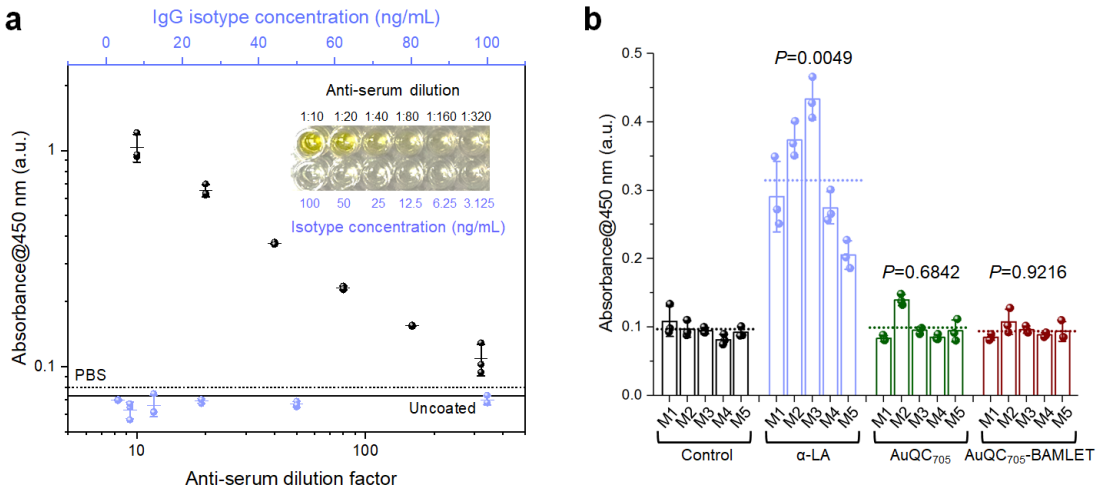

Supplementary Fig. 50 | Investigation of systemic immunogenicity. (a) Validation using an enzyme-linked immunosorbent assay (ELISA) for specific detection of produced anti-α-LA antibodies in mouse serum. Antibody titers are based on equal volume serum mixture of sera collected from all mice (n=5 biologically independent animals) injected with α-LA. Mouse IgG isotypes are used as negative controls. **(b)** Detection of specific serum anti-α-LA antibodies in mice. SPR (Supplementary Fig. 11) showed that specific binding affinity of α-LA for anti-α-LA antibody is still retained after synthesis of $AuQC_{705}$. However, the immunogenicity is significantly reduced for $AuQC_{705}$ and $AuQC_{705}$-BAMLET, mainly because the protein structure is partially unfolded during the synthesis, which is a dominant factor determining immunogenicity[16].

Supplementary References

1. Ipsen, R. & Otte, J. Self-assembly of partially hydrolysed alpha-lactalbumin. *Biotechnol Adv* **25**, 602-605 (2007).
2. Duconseille, A., Astruc, T., Quintana, N., Meersman, F. & Sante-Lhoutellier, V. Gelatin structure and composition linked to hard capsule dissolution: A review. *Food Hydrocolloids* **43**, 360-376 (2015).
3. Farris, S., Song, J. & Huang, Q. Alternative Reaction Mechanism for the Cross-Linking of Gelatin with Glutaraldehyde. *Journal of Agricultural and Food Chemistry* **58**, 998-1003 (2010).
4. Silva, R.S.G., Bandeira, S.F. & Pinto, L.A.A. Characteristics and chemical composition of skins gelatin from cobia (Rachycentron canadum). *LWT - Food Science and Technology* **57**, 580-585 (2014).
5. Tien, M.Z., Meyer, A.G., Sydykova, D.K., Spielman, S.J. & Wilke, C.O. Maximum Allowed Solvent Accessibilites of Residues in Proteins. *Plos One* **8**, e80635 (2013).
6. Royer, C.A. Probing protein folding and conformational transitions with fluorescence. *Chemical Reviews* **106**, 1769-1784 (2006).
7. Chaudhari, K., Xavier, P.L. & Pradeep, T. Understanding the Evolution of Luminescent Gold Quantum Clusters in Protein Templates. *Acs Nano* **5**, 8816-8827 (2011).
8. Venturoli, D. & Rippe, B. Ficoll and dextran vs. globular proteins as probes for testing glomerular permselectivity: effects of molecular size, shape, charge, and deformability. *Am J Physiol-Renal* **288**, F605-F613 (2005).
9. Agalioti, T.*, et al.* Mutant KRAS promotes malignant pleural effusion formation. *Nature Communications* **8**, 15205 (2017).
10. Phan, V.T.*, et al.* Oncogenic RAS pathway activation promotes resistance to anti-VEGF therapy through G-CSF-induced neutrophil recruitment. *Proceedings of the National Academy of Sciences of the United States of America* **110**, 6079-6084 (2013).
11. Sabella, S.*, et al.* A general mechanism for intracellular toxicity of metal-containing nanoparticles. *Nanoscale* **6**, 7052-7061 (2014).
12. Wu, Z. Anti-galvanic reduction of thiolate-protected gold and silver nanoparticles. *Angew Chem Int Ed Engl* **51**, 2934-2938 (2012).
13. Chaudhuri, A. & Chattopadhyay, A. Lipid binding specificity of bovine alpha-lactalbumin: a multidimensional approach. *Biochim Biophys Acta* **1838**, 2078-2086 (2014).
14. Darzynkiewicz, Z.*, et al.* Features of Apoptotic Cells Measured by Flow-Cytometry. *Cytometry* **13**, 795-808 (1992).
15. Obeid, M.*, et al.* Calreticulin exposure dictates the immunogenicity of cancer cell death. *Nat Med* **13**, 54-61 (2007).
16. Ohkuri, T.*, et al.* A protein's conformational stability is an immunologically dominant factor: evidence that free-energy barriers for protein unfolding limit the immunogenicity of foreign proteins. *J Immunol* **185**, 4199-4205 (2010).